



Article

Relative Strengths Recognition of Nine Mainstream Satellite-Based Soil Moisture Products at the Global Scale

Xiaoxiao Min ¹, Yulin Shangguan ¹, Jingyi Huang ² , Hongquan Wang ¹ and Zhou Shi ^{1,3,*} 

¹ Institute of Agricultural Remote Sensing and Information Technology Application, College of Environmental and Resource Sciences, Zhejiang University, Hangzhou 310058, China; xiaoxiaom@zju.edu.cn (X.M.); yulinsg@zju.edu.cn (Y.S.); Hongquan_Wang@zju.edu.cn (H.W.)

² Department of Soil Science, University of Wisconsin-Madison, 1525 Observatory Drive, Madison, WI 53706, USA; jhuang426@wisc.edu

³ Key Laboratory of Spectroscopy Sensing, Ministry of Agriculture, Hangzhou 310058, China

* Correspondence: shizhou@zju.edu.cn; Tel.: +86-188-5818-6616

Abstract: Soil moisture (SM) is a crucial driving variable for the global land surface-atmosphere water and energy cycle. There are now many satellite-based SM products available internationally and it is necessary to consider all available SM products under the same context for comprehensive assessment and inter-comparisons at the global scale. Moreover, product performances varying with dynamic environmental factors, especially those closely related to retrieval algorithms, were less investigated. Therefore, this study evaluated and identified the relative strengths of nine mainstream satellite-based SM products derived from the Advanced Microwave Scanning Radiometer 2 (AMSR2), Chinese Fengyun-3B (FY3B), the Soil Moisture Active Passive (SMAP), the Soil Moisture and Ocean Salinity (SMOS), and the European Space Agency (ESA) Climate Change Initiative (CCI) by using the Pearson correlation coefficient (R), R of SM seasonal anomalies (Ranom), unbiased Root Mean Square Error (ubRMSE), and bias metrics against ground observations from the International Soil Moisture Network (ISMN), as well as the Global Land Data Assimilation System (GLDAS) Noah model simulations, overall and under three dynamic (Land Surface Temperature (LST), SM, and Vegetation Optical Depth (VOD)) conditions. Results showed that the SMOS-INRA-CESBIO (IC) product outperformed the SMOSL3 product in most cases, especially in Australia, but it exhibited greater variability and higher random errors in Asia. ESA CCI products outperformed other products in capturing the spatial dynamics of SM seasonal anomalies and produced significantly high accuracy in croplands. Although the Chinese FY3B presented poor skills in most cases, it had a good ability to capture the temporal dynamics of the original SM and SM seasonal anomalies in most regions of central Africa. Under various land cover types, with the changes in LST, SM, and VOD, different products exhibited distinctly dynamic error characteristics. Generally, all products tended to overestimate the low in-situ SM content but underestimate the high in-situ SM content. It is expected that these findings can provide guidance and references for product improvement and application promotions in water exchange and land surface energy cycle.

Keywords: AMSR2; FY3B; SMAP; SMOS; ESA CCI; evaluation



Citation: Min, X.; Shangguan, Y.; Huang, J.; Wang, H.; Shi, Z. Relative Strengths Recognition of Nine Mainstream Satellite-Based Soil Moisture Products at the Global Scale. *Remote Sens.* **2022**, *14*, 2739. <https://doi.org/10.3390/rs14122739>

Academic Editor: Md Jahangir Alam

Received: 25 April 2022

Accepted: 31 May 2022

Published: 7 June 2022

Publisher's Note: MDPI stays neutral with regard to jurisdictional claims in published maps and institutional affiliations.



Copyright: © 2022 by the authors. Licensee MDPI, Basel, Switzerland. This article is an open access article distributed under the terms and conditions of the Creative Commons Attribution (CC BY) license (<https://creativecommons.org/licenses/by/4.0/>).

1. Introduction

Soil moisture (SM) is a key state variable for global land–surface interactions [1] and exerts substantial influence on water and energy cycles [2] through shunting the radiant energy into latent and sensible heat fluxes and partitioning precipitation into infiltration and runoff [3]. In the past two decades, numerous missions/sensors have been dedicated to providing large-scale and long-term SM information, including the Soil Moisture Active Passive mission (SMAP; [4]) launched by the National Aeronautics and Space Administration (NASA), the Soil Moisture and Ocean Salinity mission (SMOS; [5]) launched by the European Space Agency (ESA), the Advanced Microwave Scanning Radiometer 2

(AMSR2; [6]) onboard the Global Change Observation Mission-Water satellite (GCOM-W1), the Advanced Scatterometer (ASCAT; [7]) onboard the Metop-A/B/C, and the Microwave Radiation Imager (MWRI) onboard the Chinese FengYun (FY)-3B/C satellites [8]. In addition, the blended SM item initiated by the ESA Climate Change Initiative (CCI; [9,10]) also provides long-term and spatiotemporal continuous SM information.

Satellite-based SM products are indirectly retrieved with considerable and untraceable uncertainties. Product spatiotemporal error characteristics should be investigated and quantified through evaluation activities before launching potential applications. Currently, there are many studies exploring the skills of different SM products in distinct regions [11–15] or at a global scale [16–20]. For example, Ma et al. [17] made global comparisons of five products from SMAP, SMOS, AMSR2, and ESA CCI by investigating the impacts of five environmental factors (i.e., climate, soil roughness, spatial heterogeneity, Land Surface Temperature (LST), and Vegetation Optical Depth (VOD)) on product performance. A. Al-Yaari et al. [18] evaluated six products from SMOS, SMAP, ASCAT, and ESA CCI on different continents, land covers, and climates at the global scale. Burgin et al. [16] compared the “L2_SM_P” product from SMAP with the other four products from SMOS, ASCAT, AMSR2, and Aquarius, overall and under different land covers. Previous studies indicated that distinct assessment conclusions can be derived for the same product in different studies, which is primarily induced by the differences in product versions, data pre-processing (e.g., quality control), spatial-temporal coverage, descending/ascending orbits, assessment methods, reference datasets, and partition conditions [15,16,21,22]. Therefore, it is necessary to synchronously consider as many SM products as possible under the same contexts to uniformly obtain reliable and convincing assessment results for current mainstream products.

In addition, compared with international SM products, such as those from SMAP, SMOS, and AMSR2, the Chinese FY-3B/C-derived product has rarely been assessed globally [7], of which the relative advantages and error characteristics are widely concerned by international potential users. Cui et al. [23] and Zhu et al. [24] only evaluated the FY3B product in the Tibetan Plateau and Henan Province of China, respectively. Therefore, this study simultaneously evaluated and intercompared the FY3B product together with eight passive microwave mainstream products (i.e., the L3 Version (V)-3 AMSR2 product derived from the Japan Aerospace Exploration Agency (JAXA), the V001 C- and X-band AMSR2 products based on the Land Parameter Retrieval Model (LPRM), the L3 V6 radiometer-based SMAP product, the L3 V300 SMOS product, the V105 SMOS-IC product, and the V04.7 and V05.2 active–passive blended products from ESA CCI) at the global scale (twice the number of products investigated in most studies), spanning vast heterogeneous landscapes.

It is generally agreed that LST and VOD or Vegetation Water Content (VWC) are two critical auxiliary parameters in the passive microwave retrieval algorithms. As the static factor, the landscape has a dominant influence on SM spatiotemporal distributions at the continent or global scale [25]. Specifically, land cover (LC) is also a critical auxiliary dataset and closely related to some key algorithm input constants. Product performance under these algorithm-related factors can provide guidance for algorithm upgrades and performance improvements and, thus, they were selected as partition conditions in this study. Furthermore, to investigate the sensitivity of products to diverse SM content, SM itself was also considered as a partitioning factor. Specifically, this study investigated the dynamic changes in product performance with time-varying LST, VOD, and SM under various LC types. This two-factor crossover analysis has only been performed by Zhang et al. [26] before, but they only focused on a SMAP-derived product.

Ground observations (e.g., the SM measurements from the International Soil Moisture Network (ISMN; [27,28])) are the closest approximation to ground truth at the point scale. However, due to the sparse and uneven distributions of ground stations, the evaluation activities can only be conducted under limited and localized regions. To expand the spatial extent for product evaluation, modeled SM simulations from the Global Land Data

Assimilation System (GLDAS) Noah model are also used as a reference dataset for pixel-scale evaluation in this study, as in previous studies [29,30], to make them complementary for the in-situ evaluations and alleviate the spatial representativeness errors brought by the point-to-pixel mismatches.

Consequently, this study utilized the ground observations from ISMN networks and the GLDAS simulations together to evaluate and intercompare the performance of the JAXA AMSR2 product, the two LPRM-based AMSR2 products, the SMAP, SMOS, SMOS-IC products, and two ESA CCI products during the 2016–2018 period. The objectives are as follows: (1) identifying the relative merits of the temporal performance of each product at the global scale; (2) investigating the abilities of products in capturing SM spatiotemporal dynamics at the site and continent scales; (3) examining the influences of three dynamic environmental factors (LST, SM, and VOD) stratified by LC types on product performance. Section 2 briefly introduces the datasets, assessment metrics, and evaluation methods. Section 3 presents the evaluation and inter-comparison results. Sections 4 and 5 provide discussions and the major conclusions, respectively.

2. Datasets and Methods

2.1. Datasets

2.1.1. Satellite-Based Products

AMSR2 is onboard the GCOM-W1 satellite and provides brightness temperature (TB) information at seven microwave frequencies ranging from 6.9–89 GHz [5]. Two kinds of algorithms are, respectively, adopted by JAXA and NASA to develop relevant products. The JAXA algorithm uses the fixed LST (=293 K) and the linear relationship between VOD and VWC [31] to retrieve SM, while the NASA AMSR2 products are inversed from the LPRM [32] using the dynamic LST derived from the linear relationship with V-pol TB data at 36.5 GHz [33] and the MPDI (Microwave Polarization Difference Index)-based VOD as auxiliary parameters. To investigate the relative strengths and disadvantages brought by the algorithm and band differences, the descending (01:30 AM) L3 JAXAV3 (hereinafter called JAXA) and the V001 descending C1- and X-band LPRM-based AMSR2 (hereinafter called Lc1 and Lx) with a spatial resolution of 0.25° were both adopted. In addition, the C1-band LPRM-derived VOD estimates were also used as one of the dynamic conditions.

China launched the FY3B satellite on 5 November 2010, as the successor of the meteorological polar-orbiting satellite of FY-3A. It is equipped with the MWRI to provide TB information at five bands ranging from 10.65 to 89 GHz [34]. The dynamic LST (derived in the same way as the LPRM) and the VOD (calculated in the same way as the JAXA algorithm) information are used in the FY3B official algorithm [7]. In this study, the L3 descending product (01:40 AM) based on the 25 km Equal-Area Scalable Earth (EASE) Grid 1.0 was adopted (hereinafter called FY3B).

NASA SMAP was launched on 31 March 2015 and carries a radiometer to provide L-band TB information at the fixed incident angle (=40°; [4]). SM estimates are retrieved through the V-pol single channel (SCA-V; [35]) algorithm by using the LST information from the Goddard Earth Observing System (GEOS)-5 model and the VWC parameter derived from the Moderate-resolution Imaging Spectroradiometer (MODIS) Normalized Difference Vegetation Index (NDVI). In addition, LC information is used to partition the lookup table to select algorithm parameters, such as the single scattering albedo. The L3 V6 descending (6:00 AM) SM product (hereinafter called SMAP) and the GEOS-5 LST dataset (one of the dynamic conditions) projected on the 36km EASE Grid 2.0 [36] were adopted in this study.

ESA launched the first L-band SMOS satellite on 2 November 2009, and it is dedicated to providing SM and ocean salinity information [5]. The L-band Microwave Emission of the Biosphere (L-MEB) algorithm [37] is applied to retrieve SM. The LST simulations from the European Centre for Medium Range Weather Forecasts (ECMWF) and the VOD information initially derived by MODIS Leaf Area Index (LAI) are used for surface temperature and

vegetation corrections, respectively. The appropriate dielectric model is currently chosen by LC information. The SMOS-IC algorithm is simplified and updated based on the L-MEB algorithm [38]. The major change is the non-consideration of pixel heterogeneity to avoid uncertainties caused by the introduction of additional datasets. In addition, the newly calibrated parameters of effective vegetation scattering albedo are selected from an LC-based lookup table. The ascending (6:00 AM) L3 SMOSV3 (hereinafter called SMOS) and the SMOS-ICV105 (hereinafter called IC) both projected on the 25 km EASE Grid 2.0 were adopted in this study.

ESA CCI had blended active, passive, and combined products [8]. The V4.7 combined product is created by merging all L2 LPRM-based passive datasets (from SMMR, SSM/I, TRMM, AMSR-E, AMSR2, Windsat, and SMOS radiometers) and the TU Wien change detection-based active datasets (from ERS-1 AMI, ERS-2 AMI-WS, and ASCAT scatterometers). All the datasets are firstly rescaled into the same climatology provided by the GLDAS Noah model [39] through the Cumulative Distribution Function (CDF)-matching technique [40,41]. The V5.2 combined product includes the SMAP information compared with the V4.7 product. The emergence of more microwave SM products in the future will provide more available data sources for the CCI data fusion project. However, the performance of the blended product does not necessarily improve as the number of datasets added increases. Investigations about the influences of the newly added dataset on the blended product can provide inspiration and guidance for future CCI data fusion. Therefore, this study evaluated both the combined V05.2 and V04.7 products (hereinafter called CCI_V4.7 and CCI_V5.2) with global coverage and a spatial resolution of 0.25° . The changes brought by the addition of SMAP to the spatiotemporal accuracy of the blended product were analyzed through the comparison of the performances of the two products.

2.1.2. ISMN

As an intensive data hosting and distribution facility, the International Soil Moisture Network (ISMN) is maintained by the Vienna University of Technology and provides global in-situ observations from more than 50 operational networks and more than 2500 stations [27,28]. There were 17 networks (Table S1; 10 sparse networks and 7 dense networks) and 593 sites selected, as shown in Figure 1, after data quality control (Section 2.2.1) during the study period, with 70.8% and 18.7% of these sites concentrated in North America and Europe, respectively.

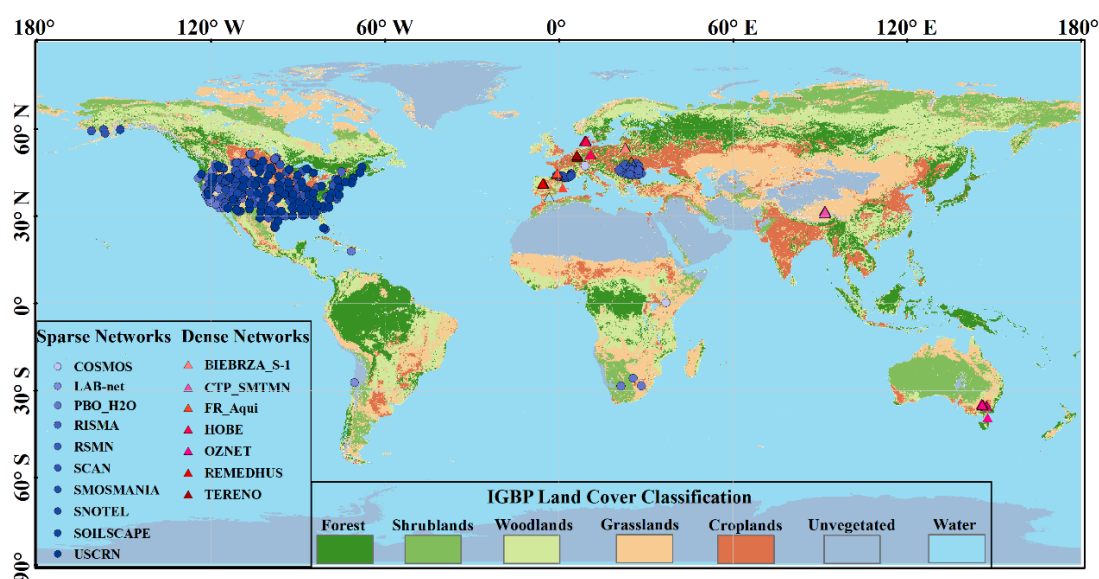


Figure 1. The global distributions of 17 ISMN networks, 593 sites, and the International Geosphere Biosphere Program (IGBP)-based land cover classification.

2.1.3. Auxiliary Datasets

The International Geosphere Biosphere Program (IGBP; [42])-based land cover map from the MODIS MCD12C1 series [43] has 18 subtypes and was reclassified into 6 primary types (Forests, Shrublands, Woodlands, Grasslands, Croplands, and Unvegetated regions), shown in Figure 1 and Table S2. The V06 2018 MCD12C1 map with a spatial resolution of 0.05° was introduced as partitions for dynamic factors in this study.

The 3 h and 0.25° GLDAS Noah simulations including SM (0–10 cm), Snow Depth (SD), and Surface Skin Temperature (SST) variables were also applied in this study. The 0–10 cm SM simulations have been adopted as references in many data merging and evaluation studies [29,30,44]. Here it was applied as a reference dataset together with the ISMN observations to perform pixel-scale and point-scale evaluations, respectively. Satellite-based SM estimates under snow and freezing conditions need to be excluded to ensure the credibility of assessment results. Therefore, the SD greater than 0 cm and SST smaller than 273.15 K were introduced as filtering criteria to eliminate abnormal SM values, according to Kim et al. [30] and Ma et al. [17].

2.2. Methods

2.2.1. Data Quality Control

Prior to implementing evaluations, preliminary quality control operations are required to obtain reliable results. Except for the above SD and SST filters, a special screening for each product was also conducted according to its quality flags (if present). For SMAP, the data were retained when the “Retrieval Quality Flag” indicated recommended quality. For SMOS, the data were excluded if the “Data Quality Index” was greater than 0.1 or the “Probability of RFI” was greater than 0.2 [45,46]. For IC, when under the two cases: (1) the “Quality Flag” was equal to 0 and (2) the “Quality Flag” and the “Scene Flag” were both equal to 1 [17]; the data were retained. For CCI V05.2, the data were adopted when the “flag” was equal to 0. For networks from ISMN, only sites with 0–10 cm measuring depth were selected (containing the maximum depth that microwaves can reach (~5 cm)) and measurements with quality flags marked as “G” [28] were retained. In addition, to reduce the impacts of system differences caused by the scale mismatches between satellite pixels and ground stations, ISMN observations were excluded when the criteria of “TC > 10%” and “WF > 10%” were both satisfied. “TC” and “WF” were the global topographic complexity and wetland fraction datasets from ESA CCI. Moreover, SM values greater than 0.6 m³/m³ were filtered out for all SM datasets [38].

2.2.2. Assessment Metrics

Four error metrics were adopted in this study: the Pearson correlation coefficient (R ; Equation (1)) to assess the product’s ability in capturing the in-situ SM temporal dynamics [47]; the Ranom (R of SM anomaly) to evaluate the product’s ability in capturing the day-to-day variation of in-situ SM [18]; the mean bias (bias; Equation (2)) to evaluate the systematic error and reflect the over- or underestimation [48], and the ubRMSE (Equation (3)) to reflect product uncertainty and random error. The descriptions of these metrics are given as follows:

$$R = E[(W_s - E[W_s])(W_g - E[W_g])] / (\sigma_s \sigma_g) \quad (1)$$

$$bias = E[W_s] - E[W_g] \quad (2)$$

$$ubRMSE = \sqrt{E\{[(W_s - E[W_s]) - (W_g - E[W_g])]^2\}} \quad (3)$$

where W_s and W_g are satellite-based and ISMN in-situ SM, respectively, σ and E are standard deviation and mean operators, respectively.

The SM seasonal cycle can unrealistically increase the degree of correlation and, thus, needs to be removed through computing the Ranom (Equation (4)) which reflects the short-scale SM temporal dynamics. Here, the SM anomalies are deviations from a 35-day

moving average [18,44]. $W_{anom}(t)$ and $W(t)$ are the anomaly and observation values at time t , and $W(t - 17, t + 17)$ is the ensemble of SM observations in the 35-day window.

$$W_{anom}(t) = [W(t) - E(W(t - 17, t + 17))] / \sigma[W(t - 17, t + 17)] \quad (4)$$

All products were collected from 1 January 2016 to 31 December 2018, and 593 sites from 17 networks were selected after data quality control. The thermal equilibrium among soil surface, vegetation, and air at nighttime is closer to the algorithm assumptions [49–51] at nighttime and, thus, only products at nighttime overpasses were adopted. The in-situ observations closest to product overpass time were selected and observations of 24 h a day were averaged for the two CCI products. For the AMSR2-based products and FY3B, the in-situ observations at 01:00 and 02:00 were averaged. To mitigate the spatial mismatches, when there were two or more sites in one pixel, ground observations from all sites in that pixel were averaged. Additionally, to maintain spatial consistency, all grids (if not 0.25°) were resampled to 0.25° by bilinear interpolation. Moreover, to comprehensively evaluate product capability in capturing SM spatiotemporal features, for each continent, both spatial and temporal error metrics were calculated. At the temporal scale, the metrics between time-series in-situ observations and satellite retrievals at each site were computed. At the spatial scale, the metrics between in-situ observations of all sites on each continent and corresponding satellite retrievals on each day were computed. To acquire robust statistical results, only datasets with a sample size (i.e., available data pairs of in-situ observations and satellite retrievals) >100 were retained. Before metrics calculations, a four-column dataset sorted by time and composed of the in-situ observations, the satellite-based retrievals, LC, and one of the dynamic conditions (LST, SM, and VOD) was prepared. For evaluations under one of the three dynamic factors partitioned by LC, the dataset was secondarily sorted by that factor and then was divided into 10 parts [26], and metrics were calculated for each part.

3. Results

3.1. Evaluations against ISMN Observations

3.1.1. Overall Evaluations

Figure 2 presents the assessment metrics for each product using the common data points from 2016 to 2018. SMAP and CCIV4.7 slightly outperformed SMOS and IC, considering R and Ranom. In addition, IC had slightly higher R and Ranom, lower ubRMSE, but larger negative bias values compared with SMOS. All metrics visibly dropped for the AMSR2-based products and FY3B, confirming the superiority of the L-band in SM monitoring compared with the C and X bands. For the AMSR2-based products, Lx exhibited higher temporal correlations with the original SM and SM seasonal anomalies (both median R and Ranom > 0.4), whereas JAXA presented lower random error (median ubRMSE < 0.12), and Lc1 showed lower systematic bias over in-situ SM (median bias ~ 0.45). The ubRMSE scores of Lc1 were also clearly higher than those of Lx. The larger random error of Lc1 may be attributed to the reason that the C band is more seriously affected by the Radio Frequency Interference (RFI; [52]) compared to the X band. Except for JAXA and Lx, other products all exhibited higher R than Ranom, indicating that these products can better capture the temporal dynamics of the original SM than those of SM seasonal anomalies. The performance of FY3B was far from satisfying with the lowest temporal correlations with the original SM and seasonal anomalies among all products. For the CCI products, the inclusion of SMAP degraded the overall performance of CCI_V5.2, considering the lower R, Ranom, and higher ubRMSE of CCI_V5.2 and SMAP, compared with CCI_V4.7. When considering the bias, JAXA exhibited significantly dry biases over in-situ SM, which was in line with the findings of Kim et al. [22]. Homoplastically, the SMOS and IC were also found to have dry biases, consistent with many previous studies [17,53].

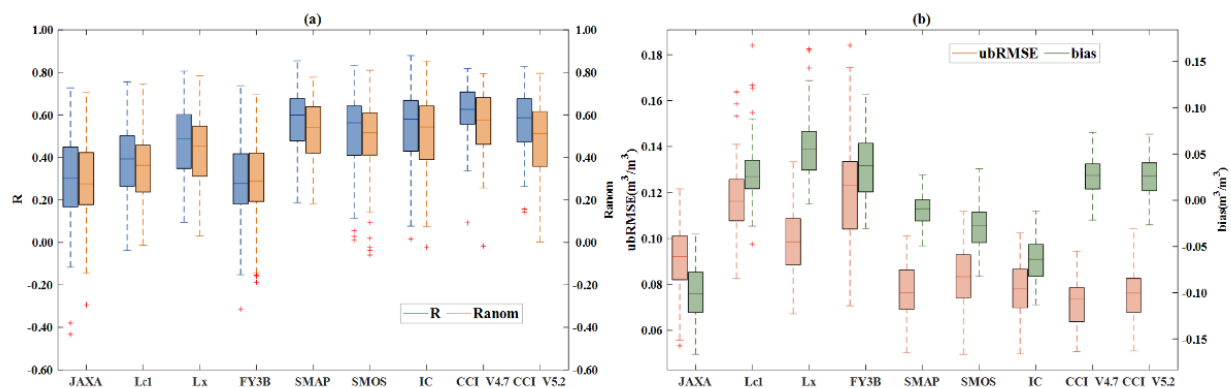


Figure 2. Boxplots of (a) R and Ranom, (b) ubRMSE, and bias against ISMN observations only considering the common data points of all products from 2016 to 2018.

To investigate the impacts of temporal sampling on the performance metric scores, all available SM retrievals for each product were also evaluated and are shown in Figure 3. IC had slightly lower temporal correlations (R and Ranom) with ISMN observations and lower ubRMSE scores than SMOS. They both had significantly poorer skills compared with the two CCI products and SMAP. In addition, the performance distinctions of the C- and X-band products from the L-band and CCI products were obvious. These findings were not in line with Figure 2 and demonstrated that temporal sampling affects the evaluation results to a certain extent [18]. Therefore, the same temporal sampling for SM retrievals from different products was required to reach more reliable inter-comparison conclusions.

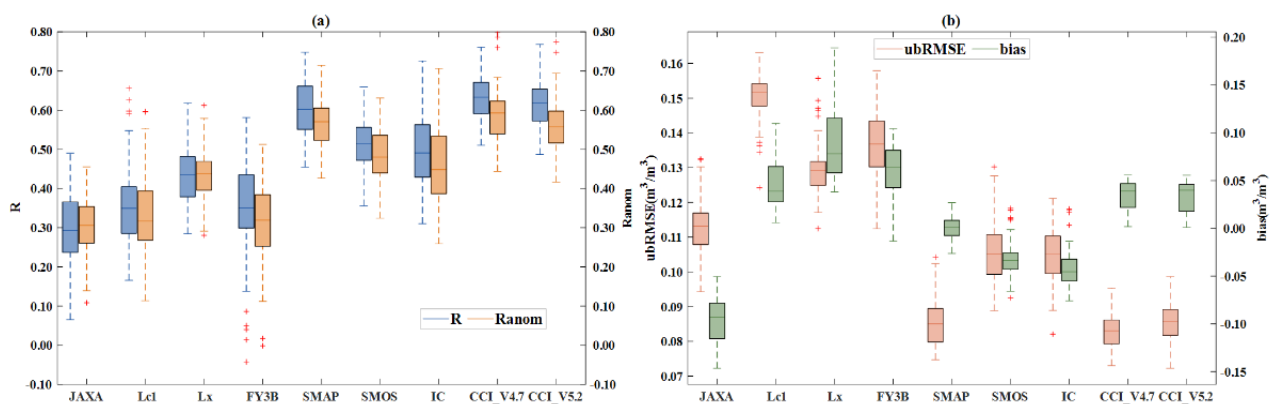


Figure 3. Same as Figure 2 but using all available SM retrievals of each product.

3.1.2. Spatial Patterns of Assessment Metrics

The spatial patterns of R, mean SM, Ranom, and Standard Deviation (SD) for each product are presented in Figures 4 and 5, respectively. In most regions of the world, Lc1 and Lx exhibited higher mean SM, followed by CCI products. However, the other products had mean SM values of $0\text{--}0.06\text{ m}^3\text{ m}^{-3}$. The lower mean SM of JAXA compared with Lc1 and Lx was possibly caused by the distinct SM ranges ($0\text{--}0.6\text{ m}^3\text{ m}^{-3}$ for JAXA versus $0\text{--}1\text{ m}^3\text{ m}^{-3}$ for Lc1 and Lx) regulated in the algorithms. Nevertheless, the higher SM estimates of Lc1 and Lx were accompanied by stronger variabilities, considering the higher SD in Figure 5b,c. In contrast, the CCI products had low SD ($0\text{--}0.05\text{ m}^3\text{ m}^{-3}$) in most of the world, even in regions with high mean SM. It proved that the multi-product fusion technique could enhance data stability to some extent. Compared with CCI_V4.7, CCI_V5.2 had drier estimates in regions above 30°N and lower variability (lower SD) in most of the world, possibly due to the inclusion of SMAP. It was worth noting that the AMSR2-based products and FY3B had stronger SM variations (higher SD) in the high-latitude regions ($>45^\circ\text{N}$), which might be related to the cold or polar climate [20], high soil organic content

(SOC; [54]), and dense vegetation (Figure 1). SOC helps to aggregate soil particles, develop soil structure, increase water storage [55] and, thus, influences soil permittivity. However, this influence is not well handled by current passive microwave retrieval algorithms. For SMOS-based products, IC had greater SM variability than SMOS in Asia, considering that it exhibited higher SD scores.

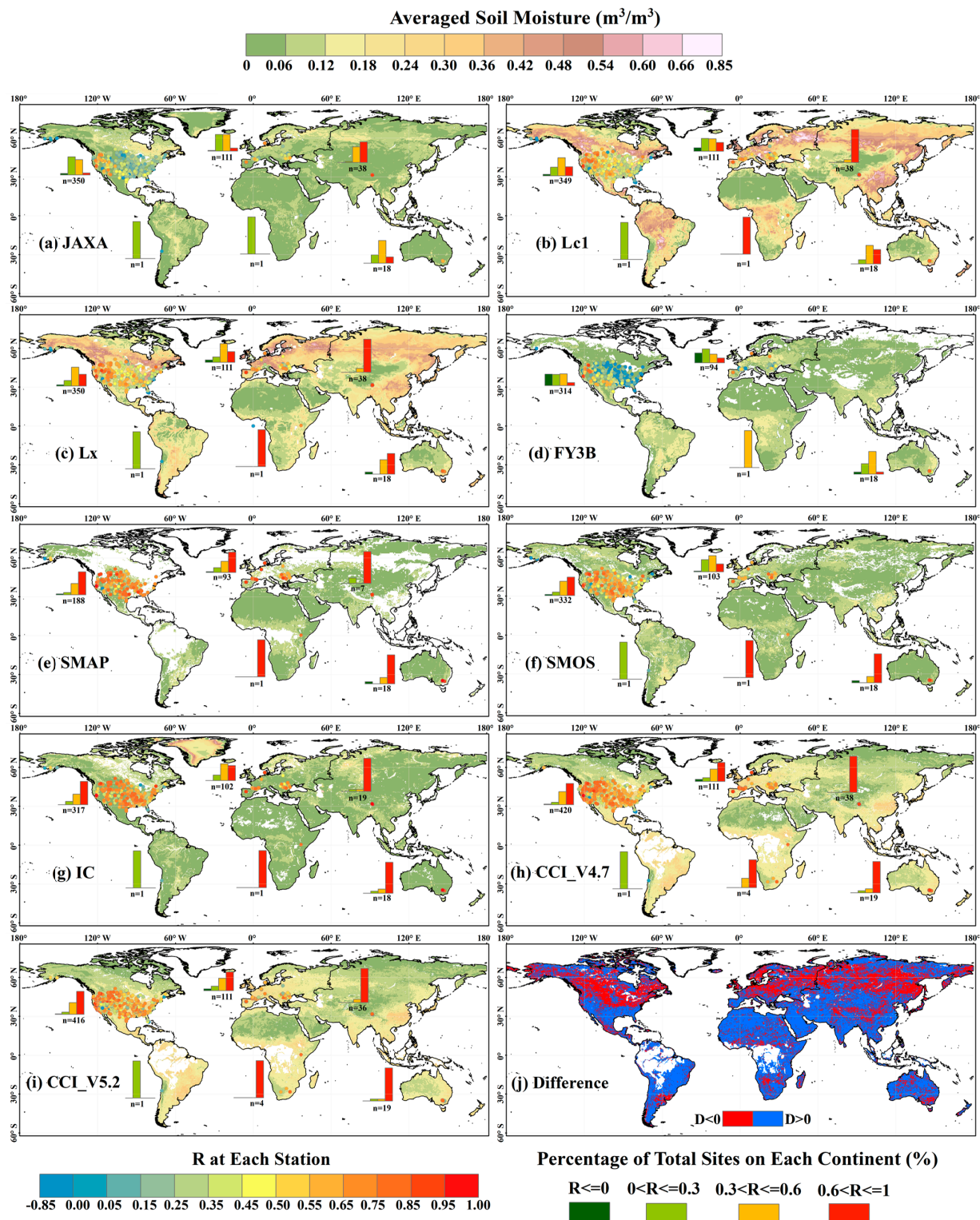


Figure 4. (a–i) are the global distributions of R and mean SM ($\text{m}^3 \text{m}^{-3}$) for each product from 2016 to 2018 (n is the number of total sites on each continent). (j) represents the difference between the averaged CCI_V5.2 and CCI_V4.7 (D means the difference).

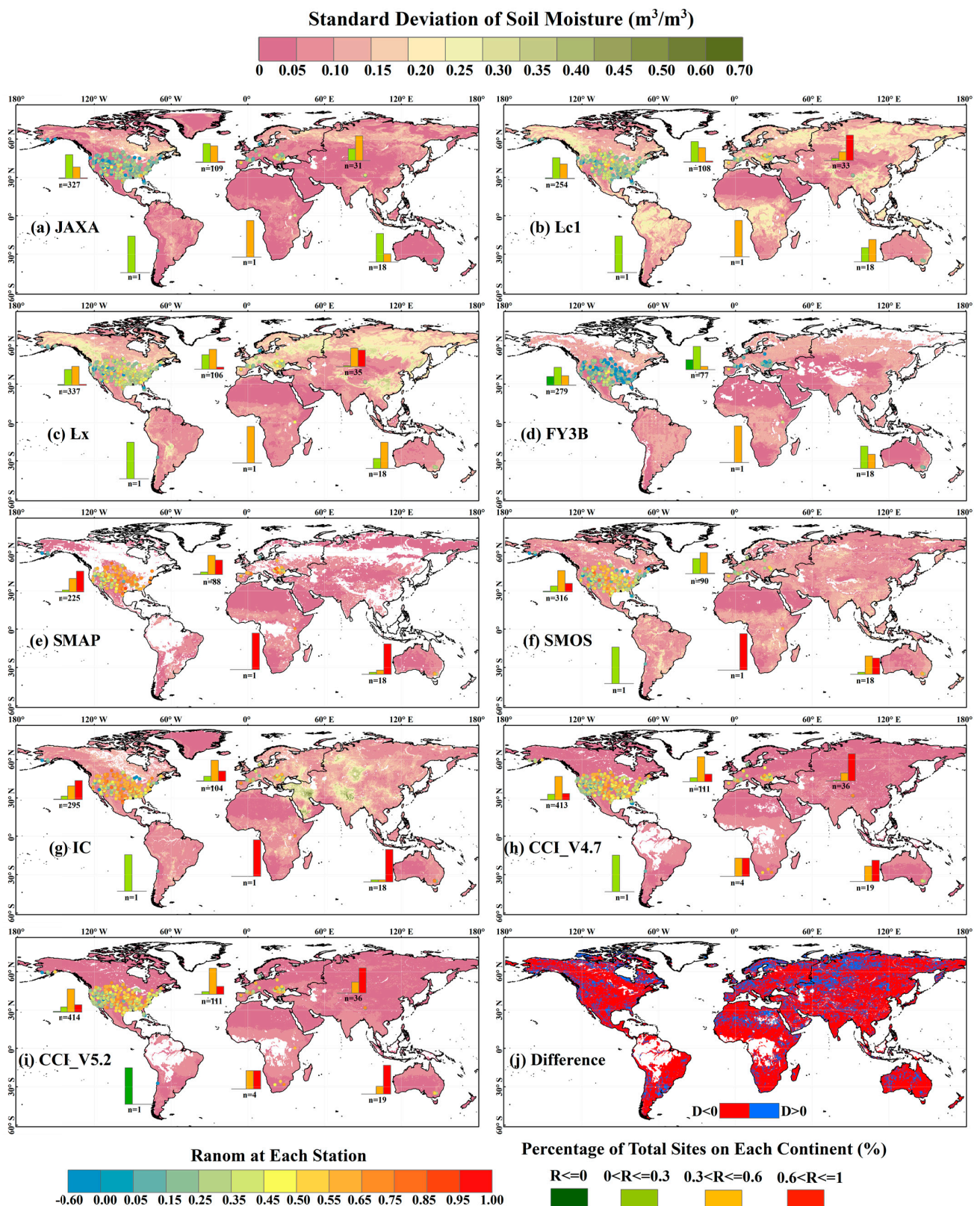


Figure 5. (a–i) are the same as Figure 4, but for global distributions of Ranom and SD for each product. (j) represents the difference between the SD of CCI_V5.2 and CCI_V4.7.

In terms of R and Ranom, JAXA and FY3B had lower temporal correlations with in-situ SM, especially in the eastern United States with $R < 0.3$ at $>50\%$ sites. SMOS and IC showed poorer accuracies in Europe with R and Ranom < 0.6 at $>50\%$ sites, which was primarily

due to the significant influence of RFI [56]. At most sites, the Ranom scores significantly decreased for all products compared with R scores, and the SMAP and CCI products could accurately capture the SM temporal dynamics with $R > 0.6$. Moreover, the AMSR2-based products and FY3B exhibited lower Ranom scores than the other products at most sites. These findings were consistent with those presented in Section 3.1.1.

3.1.3. Continent-Level Evaluations

Figure 6 shows the evaluation results for the spatial and temporal performance of each product at the continent scale. It should be noted that there is only one dense network in China (CTP_SMTMN; [57]) and Australia (OZNET; [58]), respectively. As shown in Figure 6, most products could better capture the temporal dynamics rather than spatial dynamics of both the original SM and seasonal anomalies on all continents. The reason might be that the site-to-site variation in SM was more complex than its short-term temporal variation, particularly when considering the sparse networks across vast heterogeneous landscapes. This could also explain why all products had smaller spatial random errors (ubRMSE) in the CTP_SMTMN and OZNET dense networks (distributed over small regions) than in North America and Europe. At the temporal scale, FY3B clearly exhibited the poorest performance on all continents considering all the metrics. For SMOS-based products, IC could better capture the temporal dynamics of the original SM and seasonal anomalies than SMOS on all continents. For CCI products, the CCI_V5.2 was inferior to CCI_V4.7 at the CTP_SMTMN network, considering the temporal and spatial performances of R, Ranom, and ubRMSE. However, in Europe and at the OZNET network, the CCI_V5.2 had substantially higher spatial Ranom scores than CCI_V4.7. The CCI algorithm upgrades enhanced the product's ability to capture the spatial dynamics of SM seasonal anomalies in these regions. For AMSR2-based products, although Lx outperformed JAXA and Lc1 in most cases, the two products still yielded higher spatial and temporal correlations with both original SM and seasonal anomalies in the CTP_SMTMN network, respectively, compared with Lx.

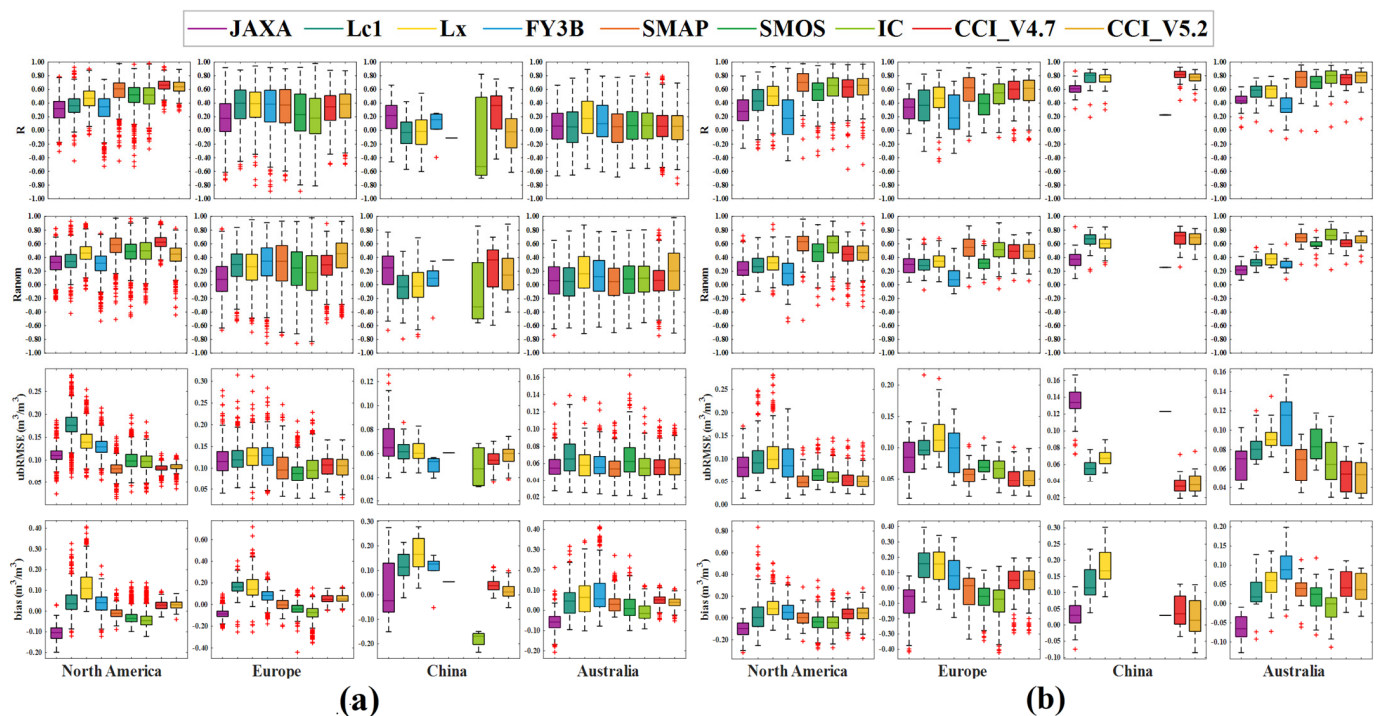


Figure 6. Boxplots of assessment metrics of each product at (a) the temporal scale (metrics calculated for each day) and (b) the spatial scale (metrics calculated for each site), partitioned by continents.

As shown in Table 1, SMAP and CCI products performed better in most instances. At the temporal scale, the optimal product in North America and Europe was SMAP, whereas

CCI_V4.7 was the optimal product in the CTP_SMTMN network. At the spatial scale, the CCI products were optimal in North America and the CTP_SMTMN network. Furthermore, the CCI products also outperformed other products considering the ability to capture the spatial dynamics of SM seasonal anomalies on all continents. Interestingly, in the OZNET network, IC exhibited better temporal performance considering R, Ranom, and bias scores, possibly due to the algorithm simplification (e.g., homogeneous pixels) and parameter improvement (e.g., soil roughness).

Table 1. The optimal product considering each spatial and temporal metric on each continent (the units of ubRMSE and bias are $\text{m}^3 \cdot \text{m}^{-3}$).

Dimensions	Metrics	North America	Europe	China	Australia
Spatial	R	CCI_V4.7	Lc1	CCI_V4.7	Lx
	Ranom	CCI_V4.7	CCI_V5.2	CCI_V4.7	CCI_V5.2
	ubRMSE	CCI_V4.7	SMOS	IC	SMAP
	bias	SMAP	SMAP	CCI_V5.2	SMOS
Temporal	R	SMAP	SMAP	CCI_V4.7	IC
	Ranom	SMAP	SMAP	CCI_V4.7	IC
	ubRMSE	SMAP	CCI_V5.2	CCI_V4.7	CCI_V5.2
	bias	SMAP	SMAP	CCI_V5.2	IC

3.2. Evaluations against GLDAS

To alleviate the contradiction of scale mismatches between in-situ observations and satellite retrievals, this study also adopted the GLDAS SM dataset as a reference to evaluate products at the pixel scale. It should be noted that the biases of CCI products are deemed meaningless and, therefore, are not shown in this section, as the two products are scaled to the same climatology provided by the GLDAS Noah model [18]. Due to the space limitation, only the R and Ranom metrics are displayed in Section 3.2.1. The performance of ubRMSE and bias can be found in the Supplemental Materials.

3.2.1. Spatial Patterns of Assessment Metrics

The spatial patterns of R (Figure 7) and Ranom (Figure 8) indicated that all products had lower temporal correlations with the original GLDAS SM and seasonal anomalies in high-latitude areas ($>45^\circ\text{N}$), featured by a cold or polar climate, high SOC, and dense vegetation. Although the performance of Ranom was significantly lower for all products compared with R (in line with Figure 2), CCI_V5.2 (Figure 8i) and SMAP (Figure 8e) still exhibited acceptable skills ($\text{Ranom} > 0.6$) in the regions outlined by green boxes (primarily distributed in America, Mexico, southeastern South America, west and southern Europe, South Africa, eastern Australia, China, and Kazakhstan). Considering the similar spatial patterns of the two products and the inferior performance of CCI_V4.7, it could be inferred that the inclusion of SMAP enhanced the capacity of CCI_V5.2 in capturing the temporal dynamics of SM seasonal anomalies. It was also worth noting that all products exhibited high R values (>0.6) in most regions of India and the 10° – 20°N regions of Africa (both outlined by yellow boxes). Moreover, the ubRMSE (Figure S1) and SD (Figure 5) metrics of most products exhibited similar spatial distributions, indicating that the strong instabilities of SM retrievals were potentially caused by high uncertainties and random errors (especially for IC, Lc1, and Lx). Compared with Lx, Lc1 had higher random errors in northern South America and central Africa (outlined by orange boxes in Figure S1b,c). Therefore, it could be inferred that the C1 band was more substantially affected by RFI in the two regions compared with the X band. Additionally, IC had significantly higher random errors and strong instabilities in the two regions outlined by the blue boxes (Figure S1g), which was likely due to the impacts of RFI.

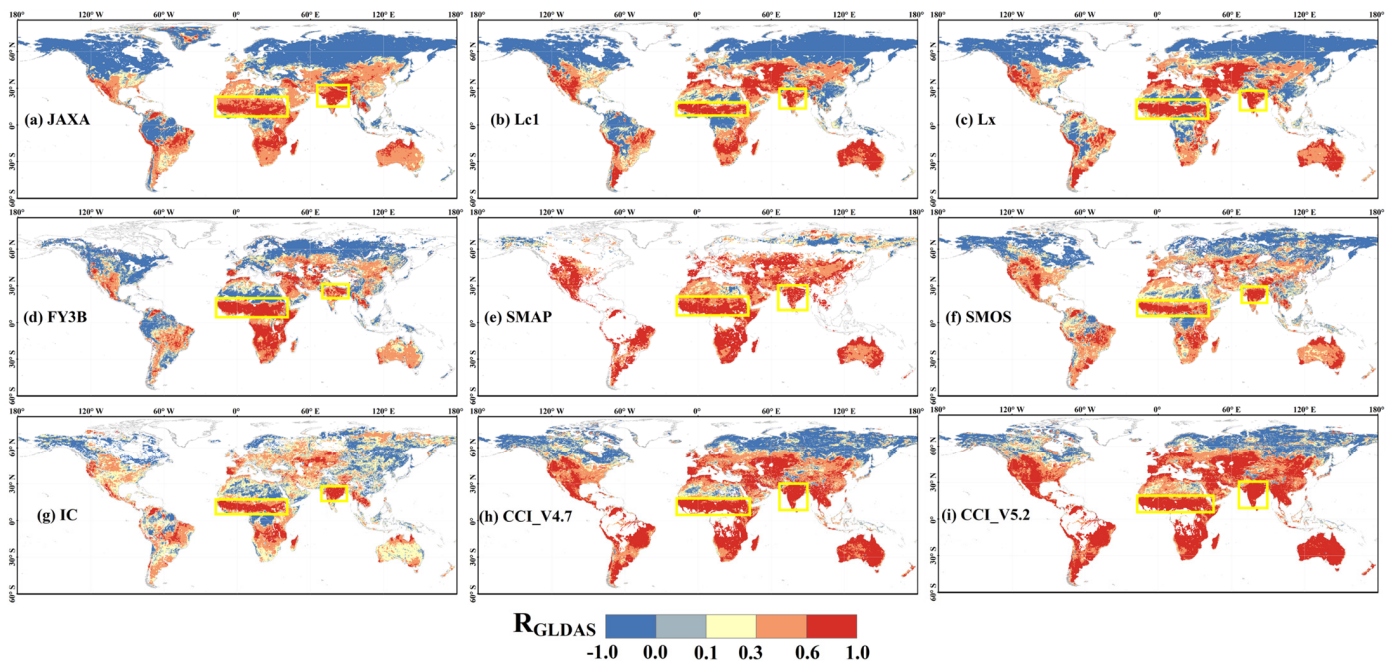


Figure 7. Spatial distribution of R against GLDAS for (a) JAXA, (b) Lc1, (c) Lx, (d) FY3B, (e) SMAP, (f) SMOS, (g) IC, (h) CCI_V4.7, and (i) CCI_V5.2. The regions with $R > 0.6$ are outlined with yellow boxes.

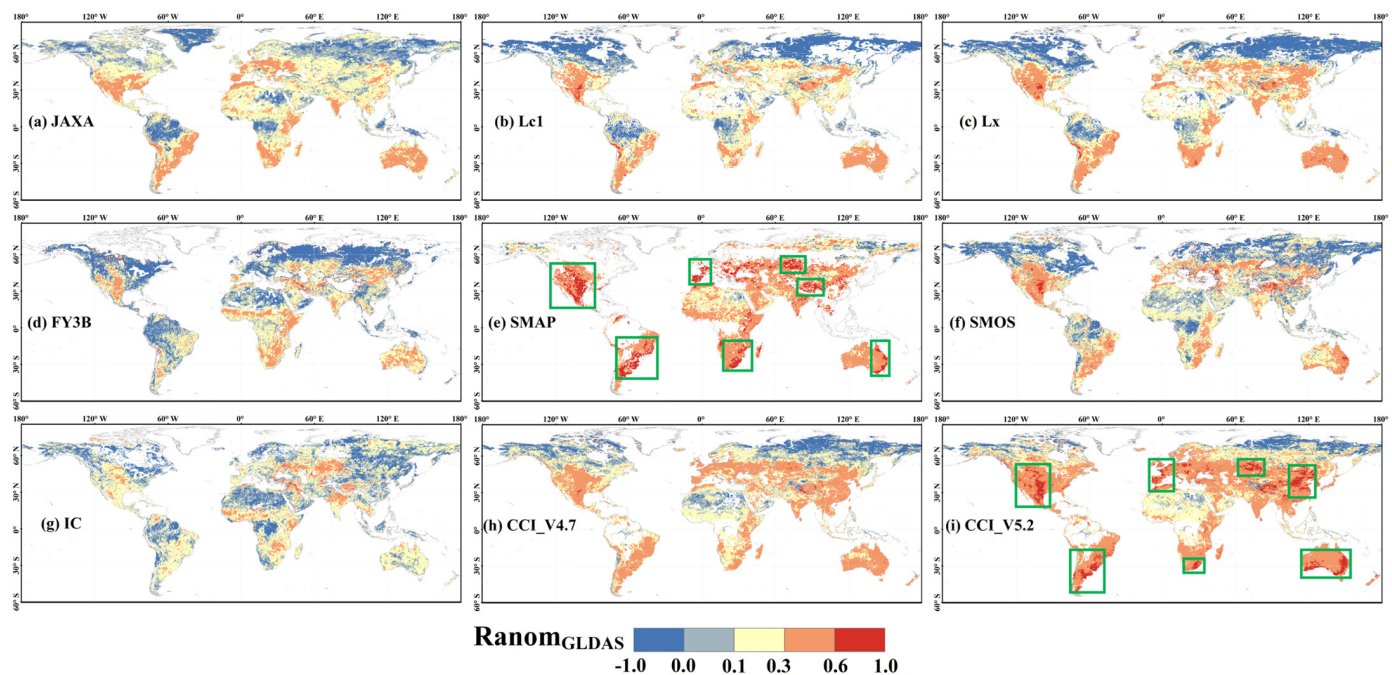


Figure 8. Spatial distribution of R_{anom} against GLDAS for (a) JAXA, (b) Lc1, (c) Lx, (d) FY3B, (e) SMAP, (f) SMOS, (g) IC, (h) CCI_V4.7, and (i) CCI_V5.2. The regions with $R_{anom} > 0.6$ of SMAP and CCI_V5.2 are outlined with green boxes.

Considering the spatial pattern of the biases (Figure S2), SMOS and IC both had higher scores, mostly in Asia and Europe. This indicated that the SMOS mission was more strongly affected by RFI on the two continents than in other regions. JAXA exhibited overestimations over GLDAS model simulations in most regions of the world (Figure S2a), which was inconsistent with Figure 2, showing that this product had a dry bias against ISMN observations. The reason might be that GLDAS had also been

found to have systematic underestimations over several ISMN networks, as confirmed by Kim et al. [30].

3.2.2. Inter-Comparisons

The comparison of the two CCI products (Figure 9A) showed that CCI_V5.2 had higher accuracy than CCI_V4.7 in most regions of the world. However, in northeast India, CCI_V4.7 outperformed CCI_V5.2 in terms of R and ubRMSE. When considering all products (Figure 9B), the CCI products had higher R and lower ubRMSE values in most regions of the world. In contrast, SMAP performed better in capturing the temporal dynamics of SM seasonal anomalies, especially in Africa and the southwestern part of Eurasia and the United States, where the advantages of this product were not fully reproduced by CCI_V5.2. The SMOS had the highest temporal correlations with the original SM and seasonal anomalies in northwest South America (outlined by red boxes). Moreover, although FY3B had poor performance in most cases compared with other products, it had the highest temporal correlations with both original GLDAS SM and seasonal anomalies in most regions of central Africa (outlined by orange boxes).

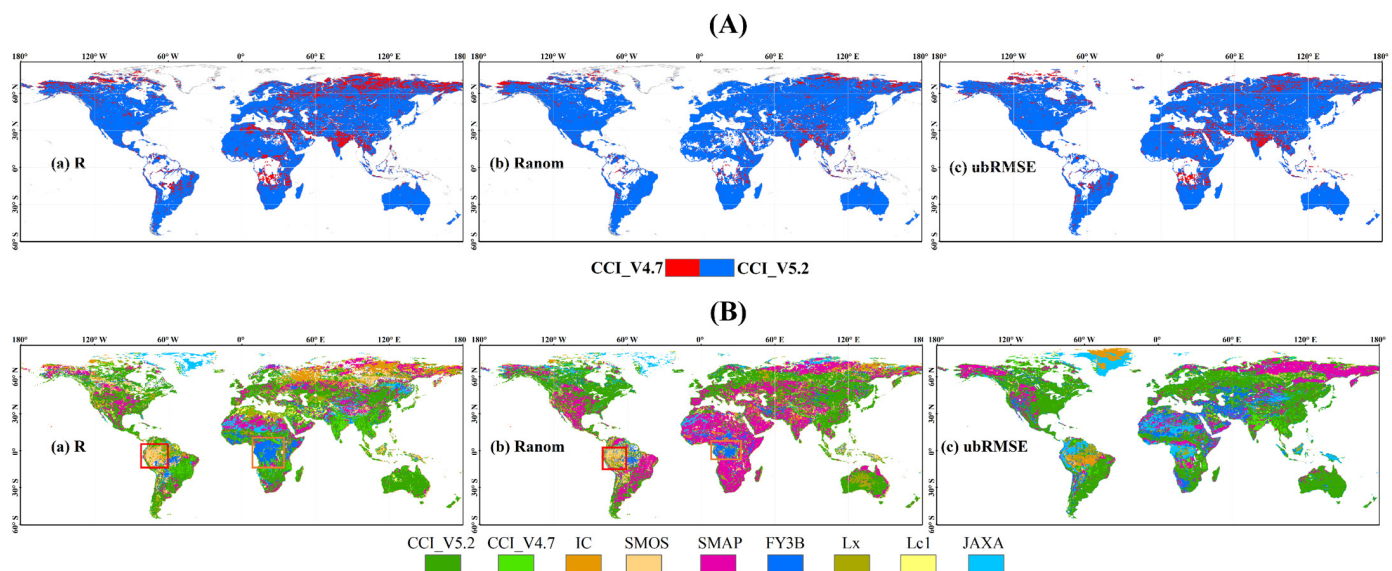


Figure 9. (A) The optimal CCI product considering (a) R (>0), (b) Ranom (>0), and (c) ubRMSE. (B) Same as (A) but considering all products and the regions where SMOS and FY3B had the best skills are outlined by red and orange boxes, respectively.

3.3. Evaluations under Dynamic Conditions

Considering the close relations of LST and VOD with passive microwave retrieval algorithms, it is necessary to investigate product performances under different LST and VOD conditions, to provide guidance for algorithm upgrades and performance improvement. Therefore, the auxiliary SMAP LST dataset from the GEOS-5 model, the C1-band LPRM-derived VOD dataset, and the ISMN in-situ observations were adopted and served as dynamic partition factors in this section. The broken lines composed of ten samples for each product are displayed under LST (Section 3.3.1), SM (Section 3.3.2), and VOD (Section 3.3.3) conditions, respectively. Previous studies seldom considered product performance under pairwise factors, especially algorithm-related factors. Zhang et al. [26] only analyzed the performance of SMAP V2 under three dynamic conditions, stratified by climates. Based on their research, the variation features of product errors with the dynamic conditions were analyzed.

3.3.1. Land Surface Temperature

Figure 10 demonstrates the performance of R, Ranom, ubRMSE, and bias for each product at various LST ranges, conditioned by six LC types. All products had similar

varying trends of R and R_{anom} with increasing LST under all the LC types. They showed the highest temporal correlations with both absolute SM and anomalies during 285 K–295 K in shrublands. SMAP had the best skills in forests and grasslands, while CCI outperformed other products in croplands considering the four metrics. In addition, the two CCI products had smaller varying ranges as LST increased under all the LC types and considering all metrics, compared with the other products. This confirmed that the data merging could reduce the impacts of LST on product performance to a certain extent. However, they had the lowest correlations at ~296 K in the unvegetated region considering both R and R_{anom} scores. It was also interesting to note that IC performed best in capturing the temporal dynamics of SM seasonal anomalies in shrublands. In addition, the AMSR2-based products and FY3B had significantly increasing R and R_{anom} scores when LST was greater than 298 K. In woodlands, SMAP had the highest performance at ~282 K, considering both R and R_{anom} , while in the unvegetated region, Lc1 and Lx had the lowest accuracy during 280 K–290 K, which indicated that the LPRM was not appropriate for SM retrieval of AMSR2 in that LST range for unvegetated soils.

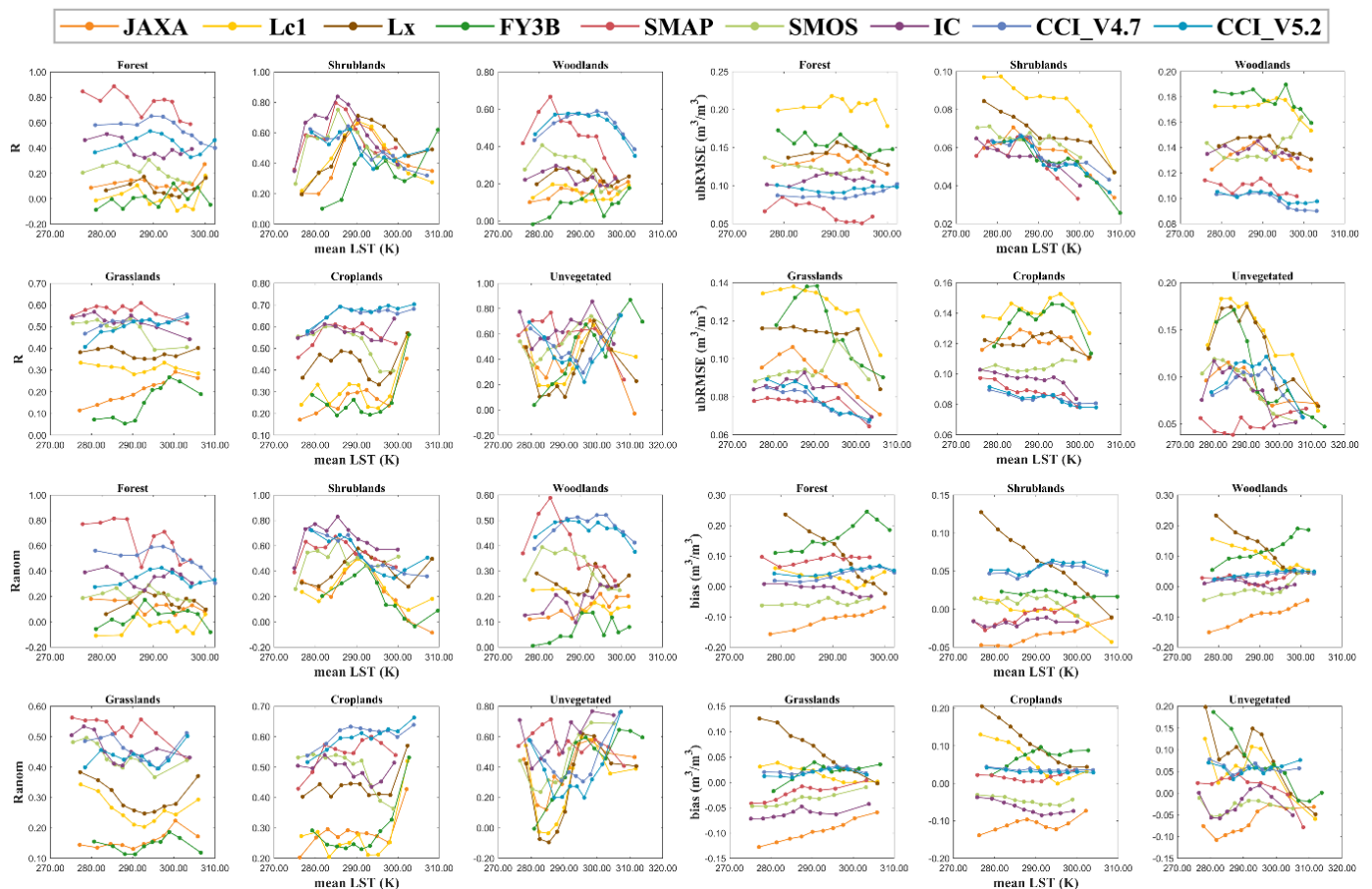


Figure 10. Line-charts of R , R_{anom} , $ubRMSE$, and $bias$ for each product varying with LST, conditioned by LC types.

In terms of $ubRMSE$, all the products had significantly decreased random errors as LST increased in shrublands. Additionally, SMAP, IC, and the two CCI products also had slightly decreased $ubRMSE$ with increasing LST in woodlands, grasslands, and croplands. In terms of $bias$, for all the LC types, JAXA significantly underestimated in-situ SM, consistent with the findings in Section 3.2.2. In addition, the underestimation was slowly relieved with increasing LST, and this similar situation was also found for IC, SMOS, and SMAP in grasslands. For Lx, the bias changed the fastest with rapidly decreasing positive bias as the

LST increased, which indicated that the bias of this product was sensitive to LST changes and the LST auxiliary parameters might be the key contributors to the systematic deviation in the AMSR2 X-band LPRM algorithm.

3.3.2. Soil Moisture

As SM increased, Figure 11 shows that all products had obvious irregular fluctuations considering R and Ranom under the six LC types. Specifically, SMAP had remarkably increasing R when SM was over $0.22 \text{ m}^3 \text{ m}^{-3}$ in forests. When SM content was above a certain threshold (i.e., in a relatively moist state), the performance of R for most products increased significantly. This was consistent with the general principle that higher SM is easier to detect, but this threshold varied significantly under various LC types ($0.35 \text{ m}^3 \text{ m}^{-3}$ in forests, $0.14 \text{ m}^3 \text{ m}^{-3}$ in shrublands, $0.21 \text{ m}^3 \text{ m}^{-3}$ in grasslands, and $0.30 \text{ m}^3 \text{ m}^{-3}$ in unvegetated regions). However, all products had decreased Ranom as SM increased in the unvegetated region. This was possibly due to the reason that increasing SM content causes the daily wetting and drying events to be less noticeable and, thus, harder for sensors to detect. It was interesting to note that SM had a smaller range ($0\text{--}0.25 \text{ m}^3 \text{ m}^{-3}$) in shrublands than in other LC types. The shrublands were primarily distributed in arid and semi-arid climates and it had been confirmed that this LC type had more bare soil and, therefore, more runoff compared with grasslands [59]. In terms of ubRMSE, most products had increasing uncertainties with increased SM in shrublands and grasslands. In terms of bias, all products had nearly linear downward trends in all the LC types with similar declining rates. As the SM increased, the wet biases gradually turned into dry biases for most products under all the LC types. This reflected a common characteristic of remote sensing SM products; namely, they tended to overestimate the low in-situ SM content but underestimate the high in-situ SM content.

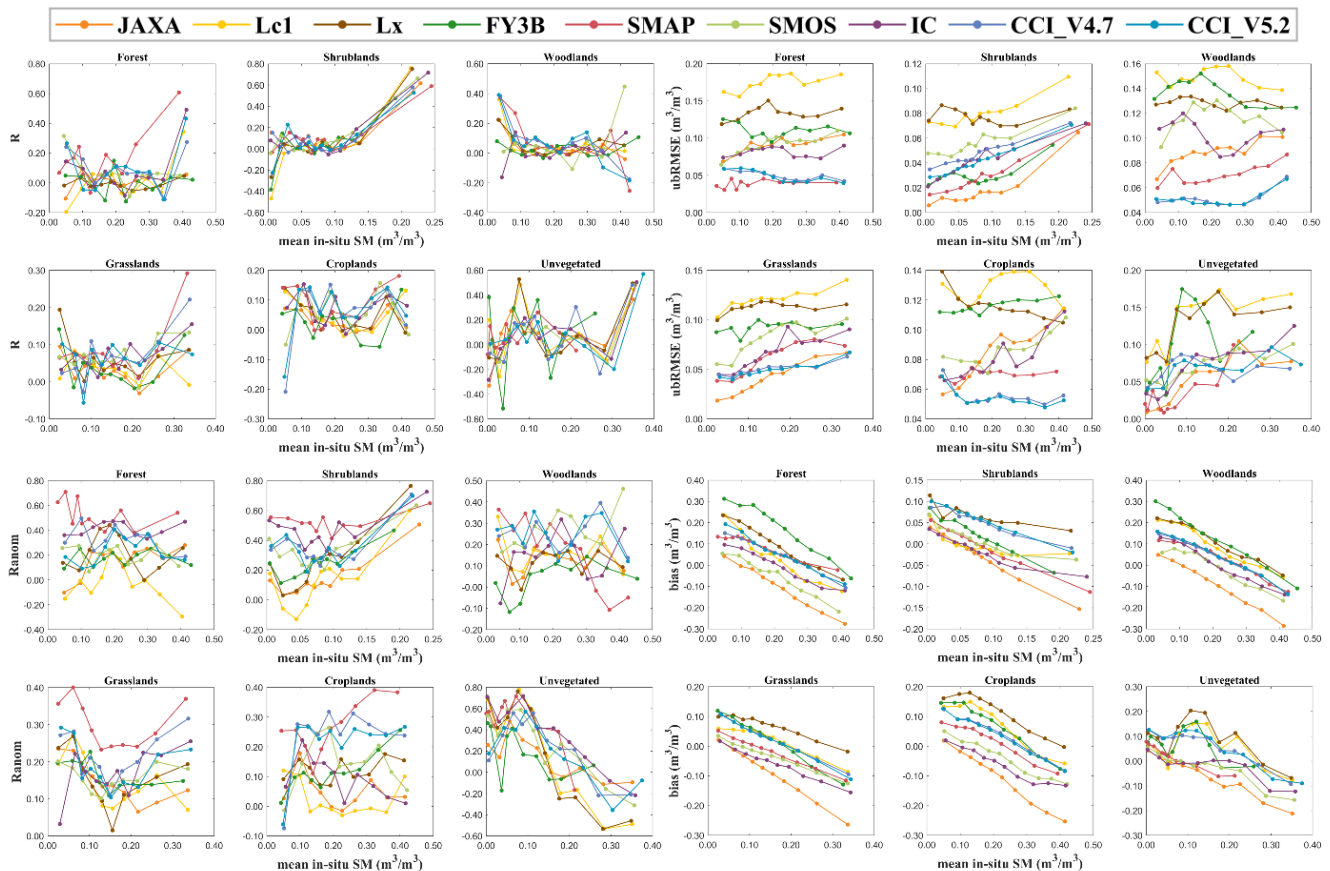


Figure 11. Same as Figure 10 but with varying SM.

3.3.3. Vegetation Optical Depth

Figure 12 shows the varying performance of each product with VOD conditioned by LC types. Due to the denser vegetation, the forest and woodlands had higher VOD than the other LC types, with a range of 0.2~1.2 and 0.2~1.0, respectively. As VOD increased, the AMSR2-based products and FY3B had slowly decreased correlations in the grasslands and croplands and showed wider variation ranges than the L-band and CCI products in most LC types, considering both R and R_{anom} . This confirmed that the C and X bands were more sensitive to the variation in VOD due to the weaker penetration capacity compared with the L-band. Most products had significantly higher performance when VOD was over 0.42 in shrublands and had two peak values (When VOD was ~0.2 and ~0.45) in the unvegetated region, considering both R and R_{anom} . In terms of ubRMSE, all the products had increasing uncertainties with increasing VOD in shrublands and had local peak values in grasslands when VOD was around 0.45. However, the ubRMSE scores remained relatively stable for all the products when VOD was over 0.42 in croplands. In terms of bias, except for Lc1, Lx, and FY3B, all the other products had slowly decreasing bias as VOD increased in grasslands, while in croplands, the bias of JAXA, SMAP, and the two CCI products remained relatively stable, whereas the negative bias of SMOS and IC gradually increased.

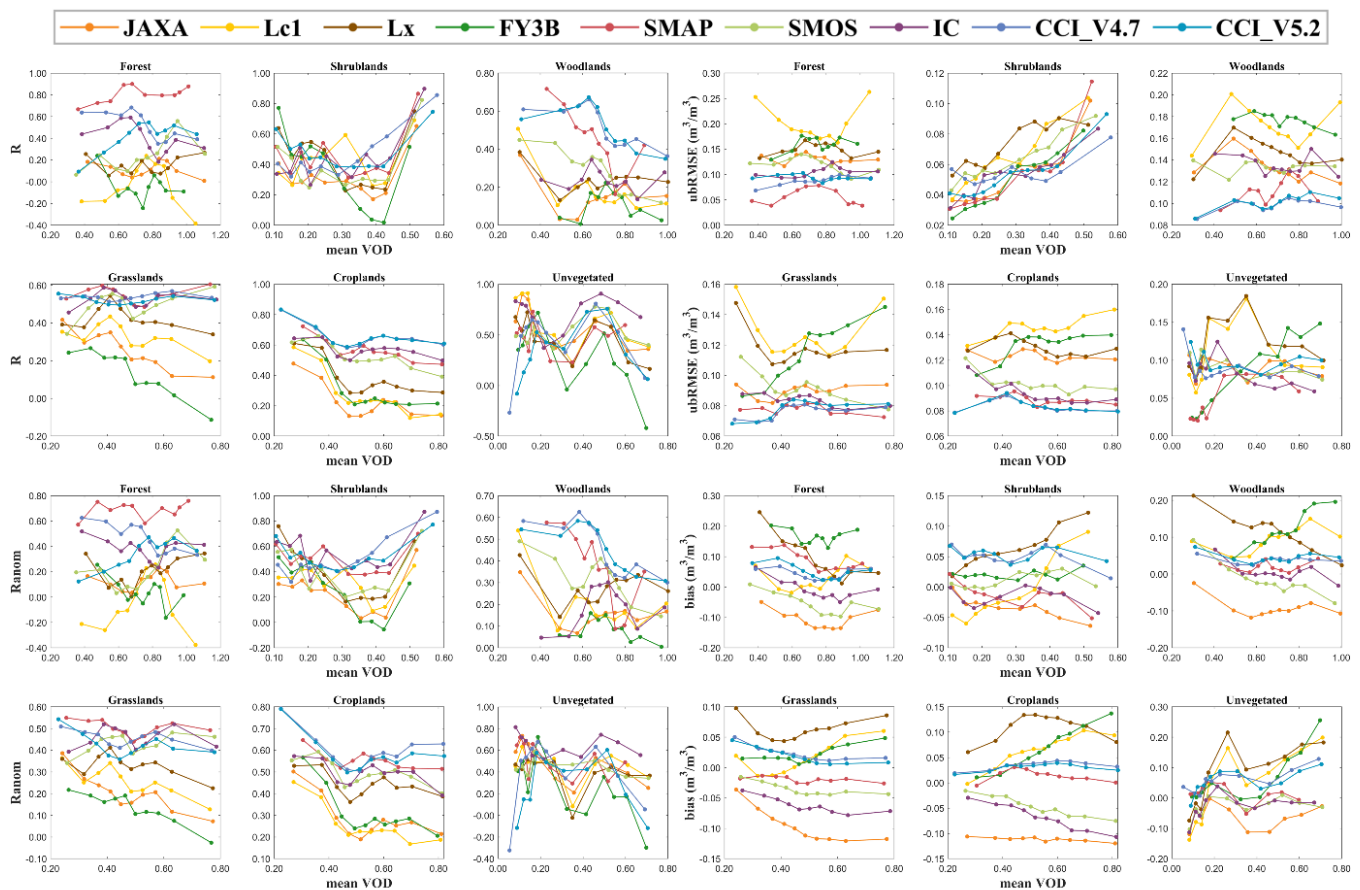


Figure 12. Same as Figure 10 but with varying VOD.

4. Discussion

The three AMSR2-based products exhibited relative strengths in terms of different metrics, as found in Section 3.1.1. The complementarity of the three products gives inspiration to the performance promotion of the AMSR2 satellite in SM monitoring, namely by combining the advantages of each product through data fusion. The FY3B had substantial room for improvement. Improving the algorithm complexity and the quality of auxiliary

parameters are effective solutions to improve product performance. For example, the empirical temperature model, which is similar to that of LPRM-based AMSR2 (LST information is derived by the empirical relationship with Ka-band TB data; [33]), should be significantly improved. As confirmed in Section 3.2.1, all the products could better capture the temporal dynamics of GLDAS model simulations in India and Africa (outlined by yellow boxes) spanning tropical and temperate climates. It had been reported that SM and precipitation were strongly coupled in climate transition zones [60]. Therefore, the SM seasonal cycle in these zones is likely more distinct and can be better captured by satellites, as confirmed by Kim et al. [22]. When the LST value was in a range from 285K to 295K, all the products exhibited higher temporal correlations with original in-situ SM and seasonal anomalies in shrublands (Section 3.3.1). SM is retrieved based on the radiative transfer model for all the passive microwave products investigated in this study. This model assumes that the soil effective temperature and vegetation temperature are approximately equal. However, this assumption is only valid if the air, vegetation, and near-surface soil are in thermal equilibrium [4,61,62]. Therefore, it could be inferred that this LST range might be the optimal temperature range in which the land–surface–atmosphere thermal equilibrium is reached. The common characteristic of all the products to overestimate low in-situ SM content but underestimate high in-situ SM content (Section 3.3.2) was due to the systematic difference caused by the different spatial representativeness between satellite pixels and the ground site. The pixel-scale satellite estimates represent an average SM status of a $\sim 25 \text{ km} \times 25 \text{ km}$ area and cannot well capture the finer point-scale SM spatial variability and, therefore, tend to exhibit smoother SM ranges than ground observations. In addition to the spatial representativeness inconsistency, there also exist systematic differences between ground and satellite measurements resulting from different measurement depths, errors in the land surface parameterization through the retrieval algorithm, and differences in sensitivity against rainfall events at the same pixel [26,63]. Although the ground observations were spatially averaged when more than one station was found in one pixel (Section 2.2.2), this operation can only partially alleviate the systematic differences. The ground observations are only the approximation of “ground truth” at the pixel scale. Therefore, special attention should be paid when interpreting the performance of the assessment metrics against in-situ observations, especially the bias metric.

In principle, the more samples, the more robust and reliable the assessment metrics are. It is unrealistic to individually select the optimal sample size for each product at each station or in each temporal range. Therefore, we set 100 as the global sample threshold (Section 2.2.2), because previous SM evaluation studies found that >100 samples were required to avoid numeric problems and ensure statistical robustness [26,29,64]. However, the sampling differences in different temporal ranges and spatial locations still cannot be avoided. For example, the satellite–ground collocated data points were fewer in forests and unvegetated regions than in the other land cover types due to the spatial distribution patterns of ISMN stations (Figure 1). The assessment metrics are based on finite samples and subject to sampling errors. As suggested by [48,65], the most common way to deal with statistical uncertainty (i.e., sampling errors) across science communities is null hypothesis significance testing using p-values and/or confidence intervals. However, the American Statistical Association confirmed that the dichotomous significance tests can lead to unjustified inferences due to strictly yet arbitrarily categorizing study results [66]. Therefore, for SM validation purposes, it is better to provide and interpret the assessment metrics in the form of confidence intervals alongside the metrics themselves [48] in future research.

Only 593 sites from the ISMN were used, which are primarily distributed in North America and Europe. The lack of sites on other continents and their uneven and sparse distributions across the globe will degrade the quality of reference datasets and limit the execution of reliable and comprehensive evaluation activities. Additionally, the GLDAS SM datasets are model simulations with considerable errors and uncertainties, which are difficult to trace and quantify, and, thus, will inevitably propagate to the evaluation

results. Therefore, the expansion of long-term, continuous ground observations and the inclusion of high-accuracy model simulations will certainly improve the reliability of evaluation results in future studies. In addition, SMAP, SMOS, and IC all use model-based auxiliary information (GEOS-5 for SMAP and ECMWF for SMOS and IC) in their algorithms, which have similar physical bases to GLDAS and, thus, probably make the metrics against GLDAS unrealistically high. However, considering that these metrics were consistent with those against ISMN, and our key concern was the relative accuracy and performance ranking of the products rather than the absolute accuracy, we still believed that it was reasonable to evaluate product performance based on the metrics against GLDAS.

Apart from LST and VOD, the impacts of other dynamic factors on product performance also need to be investigated, such as precipitation. It also controls the global water cycle and hydrological balance [67,68] and is closely related to SM dynamics. Additionally, product performance under some closely related static factors, such as climate, soil roughness, and topography, should also be investigated in future studies. The products explored in this study were based on passive microwave remote sensing and data fusion. Active microwave products, such as ASCAT-based products, should be considered in future evaluation studies to expand the assessment conclusions.

The conclusions about product performance were drawn based on the specified product versions, study regions and periods, preprocessing, data quality controls, reference datasets, assessment metrics, and result interpretations, which are critical influencing factors that should be carefully considered when selecting the optimal product for applications. Considering the diversity of environmental conditions and the multiple perspectives of product performance, this study conducted a systematic and comprehensive evaluation of mainstream satellite-based SM products, offering guidance for applications in water exchange, land surface energy, and the carbon cycle.

5. Conclusions

To comprehensively explore the accuracy and error characteristics of mainstream satellite-based SM products, our study evaluated and inter-compared nine products derived from AMSR2, FY3B, SMAP, SMOS, and ESA CCI against ISMN observations and GLDAS model simulations from 2016 to 2018. The evaluation results based on the four metrics (R, Ranom, ubRMSE, and bias) are summarized below:

- (1) In terms of the overall performance, SMAP and CCI exhibited higher accuracy compared with the other products, followed by SMOS and IC. By contrast, the AMSR2-based products and FY3B showed poorer capabilities with regard to the four metrics, especially the FY3B. In addition, JAXA, SMOS, and IC obviously featured underestimations over the in-situ SM. Temporal sampling had a certain influence on metric scores.
- (2) Most products can better capture the temporal dynamics of the original SM than those of SM seasonal anomalies and had higher temporal than spatial performance on all continents. SMOS and IC both had higher uncertainties, mostly in Asia and Europe, due to the impacts of RFI, especially in Europe with R and Ranom < 0.6 at >50% sites. The CCI products outperformed other products considering their abilities in capturing the spatial dynamics of SM anomalies on all continents. The strong variabilities (SD) in SM retrievals were typically accompanied by high random errors and uncertainties (ubRMSE), especially for IC and LPRM-based AMSR2 products.
- (3) Compared to SMOS, IC exhibited greater variability and higher random errors in Asia. However, the modification of the IC algorithm improved product performance in Australia. The CCI products had significantly high accuracy in croplands. Compared with the V4.7 product, the inclusion of SMAP enhanced the performance of the V5.2 product in most regions of the world but degraded product accuracy in northeast India. For AMSR2-based products, the Lx outperformed Lc1 and JAXA considering R in most cases. However, based on the performance of ubRMSE and bias, JAXA and

Lc1 outperformed Lx, respectively. Therefore, the integration of the three products might improve the value of the AMSR2 mission in SM monitoring.

- (4) Considering the dynamic performance with varying LST, all the products presented the highest temporal correlations with both absolutes and anomalies of SM values during 285K–295K in shrublands. In addition, the two CCI products, SMAP, and IC also presented slightly decreased ubRMSE with increasing LST in woodlands, grasslands, and croplands. Under all the LC types, the significant dry biases of JAXA were slowly relieved with increasing LST.
- (5) As SM content increased, the bias scores of all the products have nearly linear downward trends with similar declining rates under all the LC types, i.e., the wet bias over in-situ SM gradually turned into dry bias for most products under all the LC types, which revealed a common characteristic of remote sensing SM products; namely, they tended to overestimate the low in-situ SM content but underestimate the high in-situ SM content.
- (6) As VOD increased, the AMSR2-based products and FY3B had wider variation ranges in R and Ranom scores than L-band and CCI products in most LC types, which confirmed that the C and X bands were more sensitive to the variation in VOD due to weaker penetration capacity compared with the L-band.

Future remote sensing SM products will reduce error, increase monitoring accuracies, and enhance their abilities to capture SM spatiotemporal dynamics. Therefore, our findings will not only be helpful for potential product users but also provide guidance for targeted advancements in retrieval algorithms (especially model constraint improvements) and potential applications in the global water and energy cycle.

Supplementary Materials: The following supporting information can be downloaded at: <https://www.mdpi.com/article/10.3390/rs14122739/s1>, Figure S1: Spatial distribution of ubRMSE (m^3/m^3) against GLDAS for each product. The regions with distinct spatial patterns are outlined with orange boxes for Lc1 and blue boxes for IC; Figure S2: Same as Figure S1, but for bias (m^3/m^3); Table S1: List of soil moisture sites at the global scale adopted in this study [57,58,69–83]; Table S2: The IGBP land cover classification.

Author Contributions: Conceptualization, X.M. and Y.S.; methodology, X.M.; software, Y.S.; evaluation, J.H., H.W. and Z.S.; writing—original draft preparation, X.M.; writing—review and editing, Z.S.; All authors have read and agreed to the published version of the manuscript.

Funding: This research was funded by the National Key Research and Development Program (2018YFE0107000), the National Natural Science Foundation of China (41930754), and the Public Projects of Zhejiang Province (LGN18D010003). The sheep milk samples were collected as part the research programme Boosting exports of the emerging NZ dairy sheep industry (Ministry of Business of Innovation and Employment, contract no C10X1305).

Acknowledgments: We are grateful to all contributors for the datasets used in this study.

Conflicts of Interest: The authors declare no conflict of interest.

References

1. Seneviratne, S.I.; Corti, T.; Davin, E.L.; Hirschi, M.; Jaeger, E.B.; Lehner, I.; Orlowsky, B.; Teuling, A.J. Investigating soil moisture—Climate interactions in a changing climate: A review. *Earth-Sci. Rev.* **2010**, *99*, 125–161. [CrossRef]
2. Romano, N. Soil moisture at local scale: Measurements and simulations. *J. Hydrol.* **2014**, *516*, 6–20. [CrossRef]
3. Houser, P.R. Infiltration and soil moisture processes. In *Water Encyclopedia*; Keeley, J., Ed.; John Wiley & Sons, Inc.: New York, NY, USA, 2005; pp. 493–506.
4. Entekhabi, D.; Njoku, E.G.; O'Neill, P.E.; Kellogg, K.H.; Crow, W.T.; Edelstein, W.N.; Entin, J.K.; Goodman, S.D.; Jackson, T.J.; Johnson, J.; et al. The Soil Moisture Active Passive (SMAP) Mission. *Proc. IEEE* **2010**, *98*, 704–716. [CrossRef]
5. Kerr, Y.H.; Waldteufel, P.; Wigneron, J.P.; Martinuzzi, J.; Font, J.; Berger, M. Soil moisture retrieval from space: The Soil Moisture and Ocean Salinity (SMOS) mission. *IEEE Trans. Geosci. Remote Sens.* **2001**, *39*, 1729–1735. [CrossRef]
6. Okuyama, A.; Imaoka, K. Intercalibration of advanced microwave scanning radiometer-2. (AMSR2) brightness temperature. *IEEE Trans. Geosci. Remote Sens.* **2015**, *53*, 4568–4577. [CrossRef]

7. Bartalis, Z.; Wagner, W.; Naeimi, V.; Hasenauer, S.; Scipal, K.; Bonekamp, H.; Figa, J.; Anderson, C. Initial soil moisture retrievals from the METOP-A Advanced Scatterometer (ASCAT). *Geophys. Res. Lett.* **2007**, *34*, L20401. [\[CrossRef\]](#)
8. Parinussa, R.M.; Wang, G.; Holmes, T.R.H.; Liu, Y.Y.; Dolman, A.J.; De Jeu, R.A.M.; Jiang, T.; Zhang, P.; Shi, J. Global surface soil moisture from the Microwave Radiation Imager onboard the Fengyun-3B satellite. *Int. J. Remote Sens.* **2014**, *35*, 7007–7029. [\[CrossRef\]](#)
9. Liu, Y.Y.; Parinussa, R.M.; Dorigo, W.A.; De Jeu, R.A.M.; Wagner, W.; van Dijk, A.I.J.M.; McCabe, M.F.; Evans, J.P. Developing an improved soil moisture dataset by blending passive and active microwave satellite-based retrievals. *Hydrol. Earth Syst. Sci.* **2011**, *15*, 425–436. [\[CrossRef\]](#)
10. Liu, Y.Y.; Dorigo, W.A.; Parinussa, R.M.; de Jeu, R.A.M.; Wagner, W.; McCabe, M.F.; Evans, J.P.; van Dijk, A.I.J.M. Trend-preserving blending of passive and active microwave soil moisture retrievals. *Remote Sens. Environ.* **2012**, *123*, 280–297. [\[CrossRef\]](#)
11. Paulik, C.; Dorigo, W.; Wagner, W.; Kidd, R. Validation of the ASCAT Soil Water Index using in situ data from the International Soil Moisture Network. *Int. J. Appl. Earth Obs. Geoinf.* **2014**, *30*, 1–8. [\[CrossRef\]](#)
12. Griesfeller, A.; Lahoz, W.; Jeu, R.; Dorigo, W.; Haugen, L.; Svendby, T.; Wagner, W. Evaluation of satellite soil moisture products over Norway using ground-based observations. *Int. J. Appl. Earth Obs. Geoinf.* **2015**, *45*, 155–164. [\[CrossRef\]](#)
13. McNally, A.; Shukla, S.; Arsenault, K.R.; Wang, S.; Peters-Lidard, C.D.; Verdin, J.P. Evaluating ESA CCI soil moisture in East Africa. *Int. J. Appl. Earth Obs. Geoinf.* **2016**, *48*, 96–109. [\[CrossRef\]](#) [\[PubMed\]](#)
14. Fascetti, F.; Pierdicca, N.; Pulvirenti, L.; Crapolicchio, R.; Muñoz-Sabater, J. A comparison of ASCAT and SMOS soil moisture retrievals over Europe and Northern Africa from 2010 to 2013. *Int. J. Appl. Earth Obs. Geoinf.* **2016**, *45*, 135–142. [\[CrossRef\]](#)
15. Cho, E.; Su, C.H.; Ryu, D.; Kim, H.; Choi, M. Does AMSR2 produce better soil moisture retrievals than AMSR-E over Australia? *Remote Sens. Environ.* **2017**, *188*, 95–105. [\[CrossRef\]](#)
16. Burgin, M.S.; Colliander, A.; Njoku, E.G.; Chan, S.K.; Cabot, F.; Kerr, Y.H.; Bindlish, R.; Jackson, T.J.; Entekhabi, D.; Yueh, S.H. A Comparative Study of the SMAP Passive Soil Moisture Product with Existing Satellite-Based Soil Moisture Products. *IEEE Trans. Geosci. Remote Sens.* **2017**, *55*, 2959–2971. [\[CrossRef\]](#) [\[PubMed\]](#)
17. Ma, H.; Zeng, J.; Chen, N.; Zhang, X.; Cosh, M.H.; Wang, W. Satellite surface soil moisture from SMAP, SMOS, AMSR2 and ESA CCI: A comprehensive assessment using global ground-based observations. *Remote Sens. Environ.* **2019**, *231*, 111215. [\[CrossRef\]](#)
18. Al-Yaari, A.; Wigneron, J.-P.; Dorigo, W.; Colliander, A.; Pellarin, T.; Hahn, S.; Mialon, A.; Richaume, P.; Moran, R.F.; Fan, L.; et al. Assessment and inter-comparison of recently developed/reprocessed microwave satellite soil moisture products using ISMN ground-based measurements. *Remote Sens. Environ.* **2019**, *224*, 289–303. [\[CrossRef\]](#)
19. Wang, Y.; Leng, P.; Peng, J.; Marzahn, P.; Ludwig, R. Global assessments of two blended microwave soil moisture products CCI and SMOPS with in-situ measurements and reanalysis data. *Int. J. Appl. Earth Obs. Geoinf.* **2020**, *94*, 102234. [\[CrossRef\]](#)
20. Zhang, R.; Kim, S.; Sharma, A.; Lakshmi, V. Identifying relative strengths of SMAP, SMOS-IC, and ASCAT to capture temporal variability. *Remote Sens. Environ.* **2020**, *252*, 112126. [\[CrossRef\]](#)
21. Leroux, D.J.; Kerr, Y.H.; Al Bitar, A.; Bindlish, R.; Jackson, T.J.; Berthelot, B.; Portet, G. Comparison between SMOS, VUA, ASCAT, and ECMWF soil moisture products over four watersheds in US. *IEEE Trans. Geosci. Remote Sens.* **2014**, *52*, 1562–1571. [\[CrossRef\]](#)
22. Kim, S.; Liu, Y.Y.; Johnson, F.M.; Parinussa, R.M.; Sharma, A. A global comparison of alternate AMSR2 soil moisture products: Why do they differ? *Remote Sens. Environ.* **2015**, *161*, 43–62. [\[CrossRef\]](#)
23. Cui, Y.; Long, D.; Hong, Y.; Zeng, C.; Zhou, J.; Han, Z.; Liu, R.; Wan, W. Validation and reconstruction of FY-3B/MWRI soil moisture using an artificial neural network based on reconstructed MODIS optical products over the Tibetan Plateau. *J. Hydrol.* **2016**, *543*, 242–254. [\[CrossRef\]](#)
24. Zhu, Y.; Li, X.; Pearson, S.; Wu, D.; Sun, R.; Johnson, S.; Wheeler, J.; Fang, S. Evaluation of Fengyun-3C Soil Moisture Products Using In-Situ Data from the Chinese Automatic Soil Moisture Observation Stations: A Case Study in Henan Province, China. *Water* **2019**, *11*, 248. [\[CrossRef\]](#)
25. Crow, W.T.; Berg, A.A.; Cosh, M.H.; Loew, A.; Mohanty, B.P.; Panciera, R.; de Rosnay, P.; Ryu, D.; Walker, J.P. Upscaling sparse ground-based soil moisture observations for the validation of coarse-resolution satellite soil moisture products. *Rev. Geophys.* **2012**, *50*, 1–20. [\[CrossRef\]](#)
26. Zhang, R.; Kim, S.; Sharma, A. A comprehensive validation of the SMAP Enhanced Level-3 Soil Moisture product using ground measurements over varied climates and landscapes. *Remote Sens. Environ.* **2019**, *223*, 82–94. [\[CrossRef\]](#)
27. Dorigo, W.A.; Wagner, W.; Hohensinn, R.; Hahn, S.; Paulik, C.; Xaver, A.; Gruber, A.; Drusch, M.; Mecklenburg, S.; van Oevelen, P.; et al. The International Soil Moisture Network: A data hosting facility for global in situ soil moisture measurements. *Hydrol. Earth Syst. Sci.* **2011**, *15*, 1675–1698. [\[CrossRef\]](#)
28. Dorigo, W.A.; Xaver, A.; Vreugdenhil, M.; Gruber, A.; Hegyiová, A.; Sanchis-Dufau, A.D.; Zamojski, D.; Cordes, C.; Wagner, W.; Drusch, M. Global Automated Quality Control of in situ Soil Moisture data from the International Soil Moisture Network. *Vadose Zone J.* **2013**, *12*, 1–21. [\[CrossRef\]](#)
29. Dorigo, W.A.; Scipal, K.; Parinussa, R.M.; Liu, Y.Y.; Wagner, W.; de Jeu, R.A.M.; Naeimi, V. Error characterisation of global active and passive microwave soil moisture datasets. *Hydrol. Earth Syst. Sci.* **2010**, *14*, 2605–2616. [\[CrossRef\]](#)

30. Kim, H.; Parinussa, R.; Konings, A.G.; Wagner, W.; Cosh, M.H.; Lakshmi, V.; Zohaib, M.; Choi, M. Global-scale assessment and combination of SMAP with ASCAT (active) and AMSR2 (passive) soil moisture products. *Remote Sens. Environ.* **2018**, *204*, 260–275. [CrossRef]
31. Jackson, T.; Schmugge, T. Vegetation effects on the microwave emission of soils. *Remote Sens. Environ.* **1991**, *36*, 203–212. [CrossRef]
32. Owe, M.; De Jeu, R.; Holmes, T. Multisensor historical climatology of satellite-derived global land surface moisture. *J. Geophys. Res. Earth Surf.* **2008**, *113*, 1–17. [CrossRef]
33. Holmes, T.R.H.; De Jeu, R.A.M.; Owe, M.; Dolman, A. Land surface temperature from Ka band (37 GHz) passive microwave observations. *J. Geophys. Res. Earth Surf.* **2009**, *114*, 1–15. [CrossRef]
34. Yang, H.; Weng, F.; Lv, L.; Lu, N.; Liu, G.; Bai, M.; Qian, Q.; He, J.; Xu, H. The FengYun-3 Microwave Radiation Imager On-Orbit Verification. *IEEE Trans. Geosci. Remote Sens.* **2011**, *49*, 4552–4560. [CrossRef]
35. Soil Moisture Active Passive (SMAP) Algorithm Theoretical Basis Document Level 2 & 3 Soil Moisture (Passive) Data Products. 2020. Available online: https://smap.jpl.nasa.gov/documents/484_L2_SM_P_ATBD_rev_F_final_Aug2020.pdf (accessed on 30 May 2022).
36. Brodzik, M.J.; Billingsley, B.; Haran, T.; Raup, B.; Savoie, M.H. EASE-Grid 2.0: Incremental but Significant Improvements for Earth-Gridded Data Sets. *ISPRS Int. J. Geo-Inf.* **2012**, *1*, 32–45. [CrossRef]
37. Wigneron, J.-P.; Jackson, T.; O'Neill, P.; De Lannoy, G.; de Rosnay, P.; Walker, J.; Ferrazzoli, P.; Mironov, V.; Bircher, S.; Grant, J.; et al. Modelling the passive microwave signature from land surfaces: A review of recent results and application to the L-band SMOS & SMAP soil moisture retrieval algorithms. *Remote Sens. Environ.* **2017**, *192*, 238–262. [CrossRef]
38. Fernandez-Moran, R.; Al-Yaari, A.; Mialon, A.; Mahmoodi, A.; Al Bitar, A.; De Lannoy, G.; Rodriguez-Fernandez, N.; Lopez-Baeza, E.; Kerr, Y.; Wigneron, J.-P. SMOS-IC: An Alternative SMOS Soil Moisture and Vegetation Optical Depth Product. *Remote Sens.* **2017**, *9*, 457. [CrossRef]
39. Rodell, M.; Houser, P.R.; Jambor, U.; Gottschalck, J.; Mitchell, K.; Meng, C.-J.; Arsenault, K.; Cosgrove, B.; Radakovich, J.; Bosilovich, M.; et al. The Global Land Data Assimilation System. *Bull. Am. Meteorol. Soc.* **2004**, *85*, 381–394. [CrossRef]
40. Dorigo, W.; Wagner, W.; Albergel, C.; Albrecht, F.; Balsamo, G.; Brocca, L.; Chung, D.; Ertl, M.; Forkel, M.; Gruber, A.; et al. ESA CCI Soil Moisture for improved Earth system understanding: State-of-the art and future directions. *Remote Sens. Environ.* **2017**, *203*, 185–215. [CrossRef]
41. Gruber, A.; Scanlon, T.; van der Schalie, R.; Wagner, W.; Dorigo, W. Evolution of the ESA CCI Soil Moisture climate data records and their underlying merging methodology. *Earth Syst. Sci. Data* **2019**, *11*, 717–739. [CrossRef]
42. Loveland, T.R.; Belward, A. The IGBP-DIS global 1 km land cover data set, DISCover: First results. *Int. J. Remote Sens.* **1997**, *18*, 3289–3295. [CrossRef]
43. Friedl, M.A.; Sulla-Menashe, D.; Tan, B.; Schneider, A.; Ramankutty, N.; Sibley, A.; Huang, X. MODIS Collection 5 global land cover: Algorithm refinements and characterization of new datasets. *Remote Sens. Environ.* **2010**, *114*, 168–182. [CrossRef]
44. Li, D.; Zhao, T.; Shi, J.; Bindlish, R.; Jackson, T.J.; Peng, B.; An, M.; Han, B. First Evaluation of Aquarius Soil Moisture Products Using In Situ Observations and GLDAS Model Simulations. *IEEE J. Sel. Top. Appl. Earth Obs. Remote Sens.* **2015**, *8*, 5511–5525. [CrossRef]
45. Lievens, H.; Tomer, S.; Al Bitar, A.; De Lannoy, G.; Drusch, M.; Dumedah, G.; Franssen, H.-J.H.; Kerr, Y.; Martens, B.; Pan, M.; et al. SMOS soil moisture assimilation for improved hydrologic simulation in the Murray Darling Basin, Australia. *Remote Sens. Environ.* **2015**, *168*, 146–162. [CrossRef]
46. Cui, C.; Xu, J.; Zeng, J.; Chen, K.-S.; Bai, X.; Lu, H.; Chen, Q.; Zhao, T. Soil Moisture Mapping from Satellites: An Intercomparison of SMAP, SMOS, FY3B, AMSR2, and ESA CCI over Two Dense Network Regions at Different Spatial Scales. *Remote Sens.* **2018**, *10*, 33. [CrossRef]
47. Entekhabi, D.; Reichle, R.H.; Koster, R.D.; Crow, W.T. Performance Metrics for Soil Moisture Retrievals and Application Requirements. *J. Hydrometeorol.* **2010**, *11*, 832–840. [CrossRef]
48. Gruber, A.; De Lannoy, G.; Albergel, C.; Al-Yaari, A.; Brocca, L.; Calvet, J.-C.; Colliander, A.; Cosh, M.; Crow, W.; Dorigo, W.; et al. Validation practices for satellite soil moisture retrievals: What are (the) errors? *Remote Sens. Environ.* **2020**, *244*, 111806. [CrossRef]
49. De Jeu, R.A.M.; Wagner, W.; Holmes, T.; Dolman, A.; van de Giesen, N.; Friesen, J. Global Soil Moisture Patterns Observed by Space Borne Microwave Radiometers and Scatterometers. *Surv. Geophys.* **2008**, *29*, 399–420. [CrossRef]
50. Dente, L.; Ferrazzoli, P.; Su, Z.; van der Velde, R.; Guerriero, L. Combined use of active and passive microwave satellite data to constrain a discrete scattering model. *Remote Sens. Environ.* **2014**, *155*, 222–238. [CrossRef]
51. Chan, S.; Bindlish, R.; O'Neill, P.; Jackson, T.; Njoku, E.; Dunbar, S.; Chaubell, J.; Piepmeier, J.; Yueh, S.; Entekhabi, D.; et al. Development and assessment of the SMAP enhanced passive soil moisture product. *Remote Sens. Environ.* **2018**, *204*, 931–941. [CrossRef]
52. Njoku, E.G.; Ashcroft, P.; Chan, T.K.; Li, L. Statistics and global survey of radio-frequency interference in AMSR-E land observations. *IEEE Trans. Geosci. Remote Sens.* **2005**, *43*, 938–947. [CrossRef]

53. Li, X.; Al-Yaari, A.; Schwank, M.; Fan, L.; Frappart, F.; Swenson, J.; Wigneron, J.-P. Compared performances of SMOS-IC soil moisture and vegetation optical depth retrievals based on Tau-Omega and Two-Stream microwave emission models. *Remote Sens. Environ.* **2019**, *236*, 111502. [\[CrossRef\]](#)
54. De Lannoy, G.J.M.; Koster, R.D.; Reichle, R.H.; Mahanama, S.P.P.; Liu, Q. An updated treatment of soil texture and associated hydraulic properties in a global land modeling system. *J. Adv. Model. Earth Syst.* **2014**, *6*, 957–979. [\[CrossRef\]](#)
55. Liang, Z.; Chen, S.; Yang, Y.; Zhou, Y.; Shi, Z. High-resolution three-dimensional mapping of soil organic carbon in China: Effects of SoilGrids products on national modeling. *Sci. Total Environ.* **2019**, *685*, 480–489. [\[CrossRef\]](#) [\[PubMed\]](#)
56. Bircher, S.; Balling, J.E.; Skou, N.; Kerr, Y.H. Validation of SMOS Brightness Temperatures during the HOBE Airborne Campaign, Western Denmark. *IEEE Trans. Geosci. Remote Sens.* **2012**, *50*, 1468–1482. [\[CrossRef\]](#)
57. Yang, K.; Qin, J.; Zhao, L.; Chen, Y.Y.; Tang, W.J.; Han, M.L.; Lazhu, Chen, Z.Q.; Lv, N.; Ding, B.H.; et al. A Multi-Scale Soil Moisture and Freeze-Thaw Monitoring Network on the Third Pole. *Bull. Am. Meteorol. Soc.* **2013**, *94*, 1907–1916. [\[CrossRef\]](#)
58. Smith, A.B.; Walker, J.; Western, A.W.; Young, R.I.; Ellett, K.M.; Pipunic, R.C.; Grayson, R.B.; Siriwardena, L.; Chiew, F.H.S.; Richter, H.G. The Murrumbidgee soil moisture monitoring network data set. *Water Resour. Res.* **2012**, *48*, 1–6. [\[CrossRef\]](#)
59. Kurc, S.A.; Small, E. Soil moisture variations and ecosystem-scale fluxes of water and carbon in semiarid grassland and shrubland. *Water Resour. Res.* **2007**, *43*, 1–13. [\[CrossRef\]](#)
60. Koster, R.D.; Dirmeyer, P.A.; Guo, Z.; Bonan, G.; Chan, E.; Cox, P.; Gordon, C.T.; Kanae, S.; Kowalczyk, E.; Lawrence, D.; et al. Regions of Strong Coupling Between Soil Moisture and Precipitation. *Science* **2004**, *305*, 1138–1140. [\[CrossRef\]](#)
61. Hornbuckle, B.; England, A. Diurnal Variation of Vertical Temperature Gradients within a Field of Maize: Implications for Satellite Microwave Radiometry. *IEEE Geosci. Remote Sens. Lett.* **2005**, *2*, 74–77. [\[CrossRef\]](#)
62. Level 3 Active/Passive Soil Moisture Product Specification Document. 2015. Available online: https://nsidc.org/sites/files/technical-references/D72551SMAPL3_SM_PPSDVersion5.1.pdf (accessed on 30 May 2022).
63. Parinussa, R.M.; Meesters, A.G.C.A.; Liu, Y.Y.; Dorigo, W.; Wagner, W.; De Jeu, R.A.M. Error Estimates for Near-Real-Time Satellite Soil Moisture as Derived from the Land Parameter Retrieval Model. *IEEE Geosci. Remote Sens. Lett.* **2011**, *8*, 779–783. [\[CrossRef\]](#)
64. Scipal, K.; Holmes, T.; de Jeu, R.; Naeimi, V.; Wagner, W. A possible solution for the problem of estimating the error structure of global soil moisture data sets. *Geophys. Res. Lett.* **2008**, *35*, 1–4. [\[CrossRef\]](#)
65. Wilks, D.S. *Statistical Methods in the Atmospheric Sciences*, 3rd ed.; Academic Press: Cambridge, MA, USA, 2011.
66. Wasserstein, R.L.; Lazar, N.A. The ASA’s statement on p-values: Context, process, and purpose. *Am. Stat.* **2016**, *70*, 129–133. [\[CrossRef\]](#)
67. Ma, Z.Q.; Zhou, L.Q.; Yu, W.; Yang, Y.Y.; Teng, H.F.; Shi, Z. Improving TMPA 3B43 V7 datasets using land surface characteristics and ground observations on the Qinghai-Tibet Plateau. *IEEE Geosci. Remote Sens. Lett.* **2018**, *15*, 178–182. [\[CrossRef\]](#)
68. Teng, H.; Shi, Z.; Ma, Z.Q.; Li, Y. Estimating the spatial downscaled rainfall by regression kriging based on TRMM precipitation and DEM in Zhejiang Province, southeast China. *Int. J. Remote Sens.* **2014**, *35*, 7775–7794. [\[CrossRef\]](#)
69. Bell, J.E.; Palecki, M.A.; Baker, C.B.; Collins, W.G.; Lawrimore, J.H.; Leeper, R.; Hall, M.E.; Kochendorfer, J.; Meyers, T.P.; Wilson, T.; et al. U.S. Climate Reference Network Soil Moisture and Temperature Observations. *J. Hydrometeorol.* **2013**, *14*, 977–988. [\[CrossRef\]](#)
70. Bircher, S.; Skou, N.; Jensen, K.H.; Walker, J.P.; Rasmussen, L. A soil moisture and temperature network for SMOS validation in Western Denmark. *Hydrol. Earth Syst. Sci.* **2012**, *16*, 1445–1463. [\[CrossRef\]](#)
71. Calvet, J.-C.; Fritz, N.; Berne, C.; Pignat, B.; Maurel, W.; Meurey, C. Deriving pedotransfer functions for soil quartz fraction in southern France from reverse modeling. *SOIL* **2016**, *2*, 615–629. [\[CrossRef\]](#)
72. Cook, D.R. *Soil Temperature and Moisture Profile (STAMP) System Handbook*; Technical report; DOE Office of Science Atmospheric Radiation Measurement (ARM) Program: Houston, TX, USA, 2016.
73. González-Zamora, Á.; Sanchez, N.; Pablos, M.; Martínez-Fernández, J. CCI soil moisture assessment with SMOS soil moisture and in situ data under different environmental conditions and spatial scales in Spain. *Remote Sens. Environ.* **2018**, *225*, 469–482. [\[CrossRef\]](#)
74. Kristine, M.L.; Eric, E.S.; Ethan, D.G.; Andria, L.B.; John, J.B.; Valery, U.Z. Use of GPS receivers as a soil moisture network for water cycle studies. *Geophys. Res. Lett.* **2008**, *35*, L24405.
75. Leavesley, G.H.; David, O.; Garen, D.C.; Lea, J.; Strobel, M.L. A Modeling Framework for Improved Agricultural Water Supply Forecasting. In *AGU Fall Meeting Abstracts*; American Geophysical Union: Washington, DC, USA, 2008.
76. Mattar, C.; Santamaria-Artigas, A.; Duran-Alarcon, C.; Olivera-Guerra, L.; Fuster, R.; Borvar’an, D. The lab-net soil moisture network: Application to thermal remote sensing and surface energy balance. *Data* **2016**, *1*, 6. [\[CrossRef\]](#)
77. Moghaddam, M.; Entekhabi, D.; Goykhman, Y.; Li, K.; Liu, M.; Mahajan, A.; Nayyar, A.; Shuman, D.; Teneketzis, D. A Wireless Soil Moisture Smart Sensor Web Using Physics-Based Optimal Control: Concept and Initial Demonstrations. *IEEE J. Sel. Top. Appl. Earth Obs. Remote Sens.* **2010**, *3*, 522–535. [\[CrossRef\]](#)
78. Musial, J.P.; Dabrowska-Zielinska, K.; Kiryla, W.; Oleszczuk, R.; Gnatowski, T.; Jaszczyński, J. Derivation and validation of the high resolution satellite soil moisture products: A case study of the biebza sentinel-1 validation sites. *Geoinformation Issues* **2016**, *8*, 37–53.

-
79. Ojo, E.R.; Bullock, P.R.; L'Heureux, J.; Powers, J.; McNairn, H.; Pacheco, A. Calibration and Evaluation of a Frequency Domain Reflectometry Sensor for Real-Time Soil Moisture Monitoring. *Vadose Zone J.* **2015**, *14*. [[CrossRef](#)]
 80. Schaefer, G.L.; Cosh, M.H.; Jackson, T.J. The USDA Natural Resources Conservation Service Soil Climate Analysis Network (SCAN). *J. Atmos. Ocean. Technol.* **2007**, *24*, 2073–2077. [[CrossRef](#)]
 81. Wigneron, J.-P.; Dayan, S.; Kruszezski, A.; Aluome, C.; Al-Yaari, A.; Fan, L.; Guven, S.; Chipeaux, C.; Moisy, C.; Guyon, D.; et al. The aqui network: Soil moisture sites in the “les landes” forest and graves vineyards (bordeaux aquitaine region, France). In Proceedings of the IGARSS 2018-2018 IEEE International Geoscience and Remote Sensing Symposium, Valencia, Spain, 22–27 July 2018; pp. 3739–3742.
 82. Zreda, M.; Desilets, D.; Ferré Ty, P.A.; Scott, R.L. Measuring soil moisture content non-invasively at intermediate spatial scale using cosmic-ray neutrons. *Geophys. Res. Lett.* **2008**, *35*. [[CrossRef](#)]
 83. Zacharias, S.; Bogen, H.; Samaniego, L.; Mauder, M.; Fuß, R.; Pütz, T.; Frenzel, M.; Schwank, M.; Baessler, C.; Butterbach-Bahl, K.; et al. A Network of Terrestrial Environmental Observatories in Germany. *Vadose Zone J.* **2011**, *10*, 955–973. [[CrossRef](#)]